PHYSICAL REVIEW FLUIDS **6**, 043902 (2021)

Observations of a sweeping jet actuator for flow separation control of a backward-facing ramp

H. D. Lim[1,*] and Zhen Lyu[2]
[1]*Temasek Laboratories, National University of Singapore, 5A Engineering Drive 1, Singapore 117411, Republic of Singapore*
[2]*School of Aeronautic, Northwestern Polytechnical University, Xi'an 710072, China*

(Received 8 August 2020; accepted 30 March 2021; published 22 April 2021)

Flow separation control of a sweeping jet actuator in a backward-facing ramp was studied using two-dimensional and stereoscopic particle-image velocimetry. The actuator was operated at a single supply rate pertaining to a jet velocity of 7.3 m/s and positioned at the streamwise location of 0.8 and 3.7 boundary layer thickness upstream of the separating edge. Three wind tunnel reference velocities corresponding to Reynolds numbers based on the boundary layer thickness of $\mathrm{Re}_\delta = 2400$, 5200, and 9800 (jet-to-reference velocity ratios of 1, 0.5, and 0.3) were investigated, and the control effectiveness was assessed based on the size of the separation bubble. For all three Reynolds numbers, positioning the actuator nearer to the separating edge offered poorer flow separation control for measurement planes near the jet centerline. This was attributed to the upwash effect of the jet which directed high momentum fluid away from the wall leading to lower levels of entrainment, and the formation of a localized low-pressure region that coincided with the sharp change in ramp geometry leading to stronger adverse pressure gradients and lower streamwise velocities that were more likely to undergo flow reversal. At high jet-to-reference velocity ratios, the effect was accentuated, and a secondary separation bubble was observed. When the actuator was positioned further upstream, the primary streamwise vortices produced by the sweeping jet lifted away from the wall, and secondary flow structures induced near the wall contributed to higher levels of near-wall entrainment and improved flow control along the jet centerline. In contrast, for measurement planes far from the jet centerline, positioning the actuator nearer the separating edge was preferable. This was attributed to milder decay of the primary streamwise vortices, leading to stronger downwash effect and higher entrainment levels that were able to affect a wider spanwise area.

DOI: 10.1103/PhysRevFluids.6.043902

I. INTRODUCTION

The sweeping jet (SWJ) actuator is a relatively new member of active flow control (AFC) technologies and can exhibit highly unsteady spatiotemporal behavior with no need for moving mechanical parts [1]. Due to its simple design, robustness, and requirement of only a fraction of energy input that other AFC systems such as suction, blowing, and microjets may need [2–4], it has great potential in many industrial and aerospace applications. This includes flow separation control of aero vehicles, noise control of aerocomponents, heating, ventilation, and air conditioning (HVAC) technologies in buildings, film cooling, microfluidics, and jet thrust vectoring, just to name a few [5–9]. In recent years, sweeping jets have received renewed attention because of their

---

[*] Present address: Aerodynamics and Flight Mechanics Research Group, University of Southampton, Southampton SO17 1BJ, United Kingdom; hlim022@e.ntu.edu.sg

effectiveness and ease of implementation in engineering applications. This was demonstrated in a joint NASA-Boeing research effort, where the SWJ actuators were found to substantially increase the side force of a full-scale Boeing 757 vertical tail fin due to its effectiveness in flow separation control [10]. The flow properties of sweeping jets have also been characterized and the entrainment rate and total jet force was observed to be larger than a steady jet by a factor of 4 and 1.3 respectively [11]. These actuators have also been used as a miniature fluidic device for noise control of flow over a cavity [12], and were found to be particularly effective at suppressing the jet cavity tones by as much as 10 dB using mass injection levels of only 0.12% of the main jet flow.

In the context of flow separation control, SWJ actuators were found to be effective in achieving flow reattachment in a multiple flap airfoil through the formation of streamwise vortices that replaces low momentum fluid in the boundary layer with high momentum fluid from the freestream [13]. Desirable characteristics include large sweeping angles, low internal losses, and high sweeping frequencies, except for sweeping frequencies in the order of kHz, in which case the effectiveness of flow control was found to be independent of the sweeping frequency. In a subsequent study, the side force generated by a vertical tail fin model was observed to increase by more than 50% with a 2% blowing momentum coefficient, and over 20% with a momentum coefficient of 0.5% [14]. Implementation of the SWJ actuator at a pitch angle of 30 ° to the freestream direction was also studied in a wall-mounted hump model using two-dimensional unsteady Reynolds-averaged Navier-Stokes simulation, and the results showed a decrease in the size of the separation bubble for the mass flow rates that were studied [15]. For an array of SWJ actuators, an increment in the actuator spacing was found to reduce the effectiveness of flow separation control at large momentum coefficients, while sparse actuators were preferable at low momentum coefficients [10].

The SWJ actuators have also been implemented in an adverse-pressure gradient ramp application [16,17]. Its performance was benchmarked against traditional flow control techniques such as the passive microvortex generators, as well as steady and pulsed circular round jets. Through surface oil flow visualization and pressure measurements, the SWJ actuators were revealed to be the most efficient in reducing the flow separation region, and this was attributed to the generation of unsteady counter-rotating streamwise vortices over a large surface area. More recently, the SWJ actuators and steady jets were applied to a hump model, and the flow control authority was assessed based on the momentum, mass flow, and energy coefficients [18]. The SWJ actuators generally outperformed steady jets and were found to be more efficient, and this was attributed to the formation of a coherent distribution of streamwise vortices. In addition, the strength of the vortices (i.e., circulation) at the separating flow region was found to be essential in increasing the pressure recovery and reducing the flow separation region [19]. As such, a larger jet sweeping angle (110° versus 70°) was preferable as it leads to a larger skew angle that can produce streamwise vortices with higher circulation levels. Positioning the actuator closer to the separating region (2.3 versus 7 boundary layer thickness) also resulted in better performance as it minimizes the decay in vortex strength at the flow separation region.

Adjacent SWJ actuators have also been investigated in the transonic and underexpanded flow regime [20], and their results suggest that the sweeping motion is independent of their separation distance and solely determined by the geometrical design. Phase synchronization of the sweeping motion in adjacent SWJ actuators was achieved by linking the feedback channels of the actuators [21,22]. When applied to flow over a cavity, noise suppression was achieved due to control of the spanwise rolling up of the vortex sheets [21]. The internal flow dynamics and oscillation mechanism of phase-synchronized SWJ actuators have also been investigated [23], and their results showed that achieving synchronization from an asynchronous state is an extremely challenging task that may not be easy to achieve in real world conditions even if there are substantial benefits in doing so.

The ongoing developments in novel SWJ actuator design indicate that the technology is still in its early stages [24]. The flow behavior of SWJ actuators is still not well understood, and this is exemplified by the observation (and lack of explanation) of the jet separating from the nozzle exit wall when operated at high pressure ratios [20], which has a detrimental effect to flow control as it reduces the sweep angle and degrades the control effectiveness. The fundamental vortex dynamics of sweeping jets in crossflow have also been investigated with a focus on the velocity ratio and oscillation frequency [25]. However, the oscillatory patterns, sweep angle, and compressibility effects, which are expected to have strong influences on the vortex dynamics and efficacy of separation control, were not considered and were left for future studies.

The current study is on the application of a single SWJ actuator for flow separation control of a backward-facing ramp in a wind tunnel for a Reynolds number of $\mathcal{O}(10^4)$ based on the ramp height. Two-dimensional planar (2D-2C) and stereoscopic (2D-3C) particle-image velocimetry (PIV) were performed in the streamwise and cross-stream planes respectively, and the actuator's streamwise position and Reynolds number were varied systematically. The flow past a backward-facing ramp is one of the classic examples of a separated boundary layer and was selected because it allows for meaningful comparisons with literature of other AFC techniques. Examples include synthetic jet studies (zero-net-mass-flux jets) which can produce pulsed jets at prescribed frequencies to control the separating flow [26], or plasma synthetic jet actuators which have the advantages of no moving part and additional mass injection [27].

The current study aims to address the following literature gaps: (1) The majority of the existing SWJ flow control studies were performed for a Reynolds number of $\mathcal{O}(10^5\text{–}10^7)$ [10,15,18,19], which falls within the fully turbulent regime relevant to high speed airfoils applications. The current work bridges the gap to low-speed airfoils that tend to operate in the laminar to transitional-turbulent regime with a Reynolds number of $\mathcal{O}(10^4\text{–}10^5)$ [28], and can be found in applications such as microair vehicles (MAVs) and unmanned aerial vehicles (UAVs). (2) Most flow separation control studies are focused on an array of actuators at relatively high actuation frequencies to generate spanwise or streamwise vortices with spanwise uniformity [18,29]. The current study focuses on a single SWJ actuator in a configuration designed to produce three-dimensional flow features at a very low sweeping frequency of $\mathrm{St_H} = 0.09$ (based on the ramp height). (3) There is limited spatially resolved experimental data of SWJ actuators for flow separation control, particularly for the chosen configuration in the current study, resulting in a lack of information on the three-dimensional features of the separation bubble and a lack of high-fidelity experimental data to validate numerical solutions. The current study presents spatially resolved PIV results in the streamwise and cross-stream planes.

II. EXPERIMENTAL SETUP

A. Wind tunnel facility and ramp model

The experiments were performed in the small-scale blowdown wind tunnel of Temasek Laboratories at the National University of Singapore (TL@NUS). The wind tunnel can operate up to 35 m/s with a general turbulence intensity of below 0.25%. The cross section of the test section measured 160 mm × 160 mm and the length was 750 mm. A backward facing two-dimensional (2D) ramp model with height of $H = 25$ mm was used to create the separating flow and was designed based on previous flow separation control studies [27,30,31]. Key dimensions of the ramp model are provided in Fig. 1. The ramp model was designed with a hollow cutout which allowed flow control actuators of standard dimensions to be installed or removed without changing the entire ramp model.

Following the practices of an earlier study [32], the reference velocity (U_{ref}) of the main flow was taken at a location before the separating edge ($x/H = -0.5$ for the current study). Three reference velocities of $U_{\mathrm{ref}} = 7.4$, 15.1, and 25.1 m/s were investigated, which correspond to Reynolds numbers based on the ramp height (i.e., $H = 25$ mm) of $\mathrm{Re_H} = 1.2 \times 10^4$, 2.5×10^4, and 4.1×10^4 and Reynolds numbers based on the boundary layer thickness of $\mathrm{Re}_\delta = 2400$, 5200, and 9800 respectively. Note that the boundary layer thickness was determined based on the definition of $0.99U_{\mathrm{ref}}$ and from velocity profiles extracted from ensemble- averaged PIV results of the ramp model setup without any flow control devices installed. The averaged boundary layer thickness across all three wind tunnel reference velocities was $\delta_{\mathrm{avg}} = 5.33$ mm with an estimated uncertainty of ±0.41 mm. The SWJ actuator was introduced at two different streamwise positions, corresponding to $0.9D$ and $3.9D$ upstream of the separating edge (i.e., $x/D = -0.9$ and $x/D = -3.9$), where $D = 5$ mm

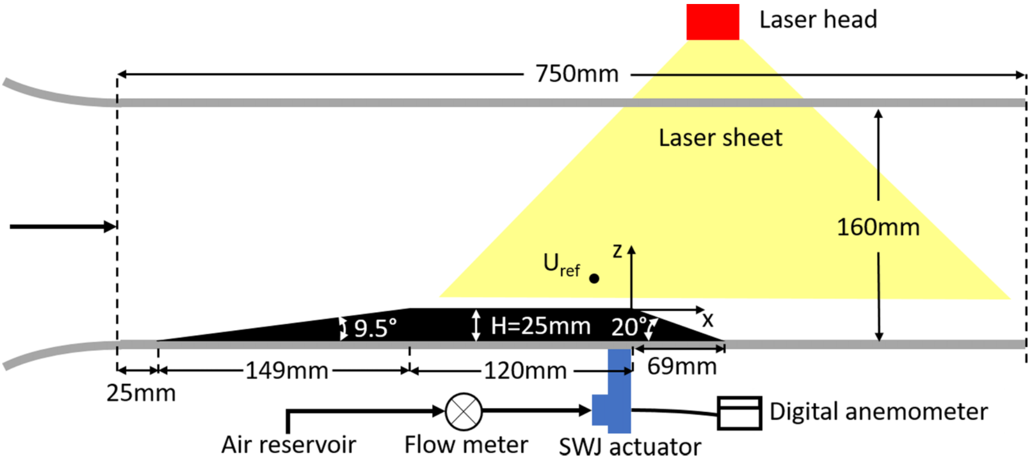

FIG. 1. Schematic of the experimental setup during 2D PIV measurements.

represents the hydraulic diameter of the SWJ actuator. These two positions are also equivalent to approximately $0.8\delta_{\mathrm{avg}}$ and $3.7\delta_{\mathrm{avg}}$ upstream of the separating edge respectively.

B. Particle-image velocimetry

Two-dimensional PIV was performed to obtain the xz plane (streamwise) velocity fields at the $y/D = 0$, 1, 2, and 3 locations. No measurements were made beyond $y/D = 3$, as the single sweeping jet actuator was designed to control the separation and attachment nodes near the centerline and not the spiral nodes near the walls. A 200 mJ/pulse, double-pulsed Litron Nd:YAG laser was used to produce a laser sheet with thickness of approximately 1 mm and aligned with the xz plane as shown in Fig. 1. The flow field was seeded with oil droplets at the inlet of the wind tunnel, and the nominal diameter of the seeding particles was 1–3 μm. A Phantom Miro 320S with 1920 × 1200 image resolution fitted with a Nikon AF DC Nikkor 105 mm f/2D lens was used to capture the particle images. The triggering events were controlled with an inhouse LABVIEW software. For a single test case, 3540 image pairs were captured at an acquisition rate of 10 Hz. The interframe time for a single image pair was between 20 and 60 μs depending on the exact test case, and extra care was taken to ensure optimal particle displacements based on the required vector resolution and interrogation window sizes. The particle images were postprocessed with an open source MATLAB package, PIVlab 2.3.1 [33], which had been used in several fluid flow studies involving 2D PIV measurements [34,35]. A two-pass multigrid cross-correlation analysis was performed with an overlap ratio of 50% throughout, and the initial and final interrogation window sizes were 32 px × 32 px and 16 px × 16 px respectively. Global and local thresholds were used to detect spurious vectors, and a three-point by three-point neighborhood interpolation scheme was used to replace the spurious vectors. The final vector resolution was 0.82 mm (approximately $0.033H$ or $0.16D$). The measurement uncertainties (based on freestream) of the normalized velocity components (i.e., U/U_{ref} and V/U_{ref}) for the three wind tunnel reference velocities were between 1.6 and 1.8% for a 95% confidence interval.

For the stereoscopic PIV setup, two Phantom Miro 320S fitted with Schneider PC TS Makro-Symmar 90 mm f/4.5 lens were used to capture the particle images, as shown in Fig. 2. The laser equipment, triggering software, and seeding particles were the same as the 2D PIV experiments. The laser sheet thickness is estimated to be approximately 2 mm and was aligned with the yz plane at several streamwise locations, although only results associated with the measurement plane at $x/H = 0.2$ will be presented. The interframe times were varied between 15 and 40 μs (depending on the wind tunnel reference velocities) to ensure optimal particle displacements in all three spatial

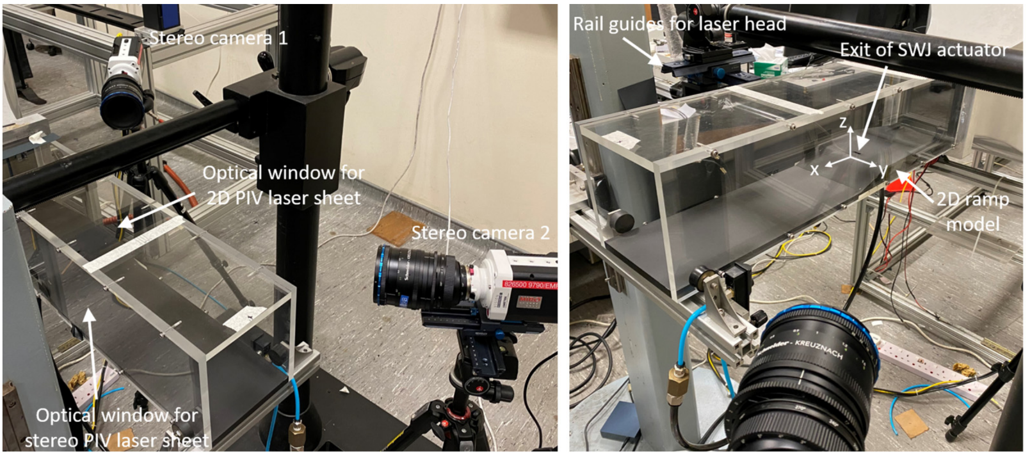

FIG. 2. Images of the experimental setup during stereoscopic PIV measurements.

directions. A bespoke external calibration board was aligned with the laser sheet in order to calibrate the extrinsic parameters of the cameras as accurately as possible. Misalignments of the calibration plate with the laser sheet was difficult to completely eliminate in practice and has also been reported in literature [36]. The authors estimate a calibration error of approximately 2 mm in the x and y directions (thickness of the laser sheet from the Litron Nd:YAG laser and the laser alignment tool) and 1 mm in the z direction.

For postprocessing, a combination of open source MATLAB packages (PIVlab and UVMAT [37]) was used to improve efficiency and reduce computational time. An inhouse MATLAB algorithm was also used to ensure compatibility between the open source MATLAB packages. The particle images were postprocessed using two-pass multigrid cross-correlation analysis with initial and final interrogation window sizes of 48 px × 48 px and 24 px × 24 px, to achieve a vector resolution of around 0.7 mm. Standard global and local thresholds were used to detect the spurious vectors, which were then replaced using a three-point by three-point neighborhood interpolation scheme. Stereoscopic reconstruction of the velocity fields was then performed by projecting the velocity fields onto an yz plane (initialized with 0.5 mm vector resolution) using the linear interpolation scheme. The measurement uncertainties (based on freestream) of the normalized velocity components (i.e., U/U_{ref}, V/U_{ref}, and W/U_{ref}) for the test cases were between 1.3% and 2.2% for a 95% confidence interval.

C. Characterization of sweeping jet actuator

The SWJ actuator was designed with a square throat that measured 5 mm × 5 mm (hydraulic diameter of $D = 5$ mm), a nozzle divergent or opening angle of approximately 100°, and exit dimensions of 17.8 mm × 5 mm (see Fig. 3). It was mounted within the ramp model and oriented such that the sweeping motion was in the y direction and orthogonal to the main flow as shown in Fig. 3. In order to characterize the SWJ actuator, the supply rate and sweeping frequency were measured simultaneously using a flow meter and constant temperature hot-wire anemometry (HWA). At a supply rate of $Q = 11$ liters/min, the velocity at the nozzle throat was approximately $U_{\mathrm{jet}} = 7.3\,\mathrm{m/s}$ assuming a top-hat velocity profile. The sweeping frequency was $f_{\mathrm{osc}} = 26.9$ Hz, and was found to increase linearly with the supply flow rate (i.e., U_{jet}) of the actuator, which agreed well with the results of past SWJ studies in the absence of compressibility effects [11,38]. The corresponding jet Strouhal number based on the sweeping frequency, hydraulic diameter, and throat velocity was

$$\mathrm{St}_{\mathrm{jet}} = \frac{f_{\mathrm{osc}} D}{U_{\mathrm{jet}}} = 0.018. \tag{1}$$

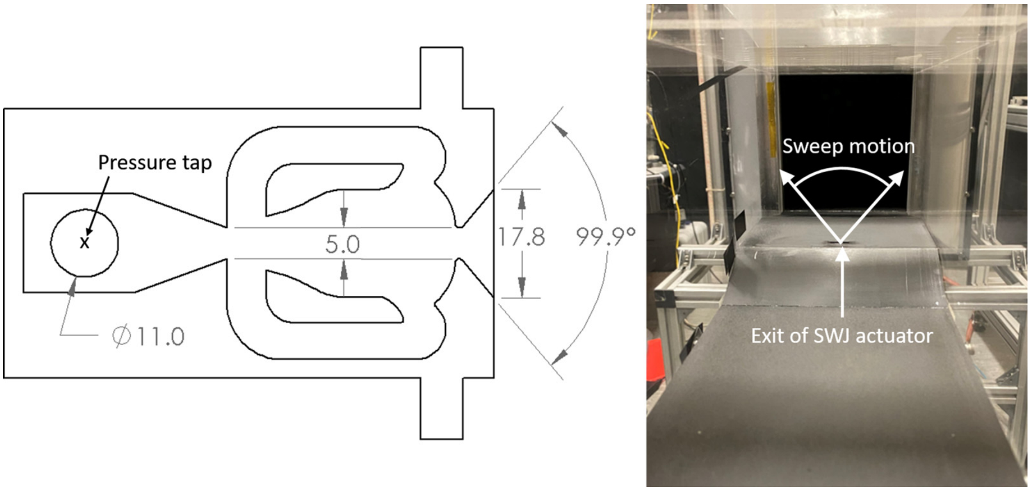

FIG. 3. Schematic of the sweeping jet actuator and its mounting configuration in the wind tunnel. Dimensions are in millimeters.

For a fixed SWJ actuator design, it was not possible to vary the Strouhal number without modifications to the length of the feedback channels or the geometry of the wall attachment region in the cavity. Hence, all experiments were performed with a constant flow rate of $Q = 11$ liters/min, and the freestream velocity of the wind tunnel was varied instead to create different velocity ratios and Reynolds number.

The jet-to-reference velocity ratio (VR) is defined as

$$\mathrm{VR} = \frac{U_{\mathrm{jet}}}{U_{\mathrm{ref}}} \tag{2}$$

and was approximately 1, 0.5, and 0.3 for the three reference velocities of $U_{\mathrm{ref}} = 7.4$, 15.1, and 25.1 m/s that were investigated. From a practical standpoint, it also made sense to vary the velocity ratio by adjusting the reference velocity, as it represents the performance of a fixed SWJ actuator design when subjected to changes in the flight conditions. During the experiments, a CEM DT-8920 digital anemometer was used to monitor the internal chamber gauge pressure with the pressure tap located at the center and directly opposite the supply inlet (see Figs. 1 and 3). This ensured that the SWJ actuator was always operated at the same conditions throughout the experiments. These data were also used to provide the boundary conditions for subsequent numerical studies.

The momentum coefficient is another useful parameter to characterize the SWJ actuator and can be defined as

$$C_\mu = \frac{\dot{m} U_{\mathrm{jet}}}{q_\infty S}, \tag{3}$$

where $\dot{m}$ represents the mass flow rate of the jet, q_∞ is the dynamic pressure of the wind tunnel, and S is the model planform area. Using the reference velocity for the freestream velocity and considering that the flow is incompressible, this is reduced to

$$C_\mu = \frac{2A_n}{S}(\mathrm{VR})^2 \tag{4}$$

The current study was performed on a 2D ramp model but involved a SWJ actuator that can produce three-dimensional (3D) flow fields due to its sweeping motion, very much similar to the experiments performed by Koklu [19]. As such, instead of using the product of the width and length of the ramp model to compute the model planform area, it is more appropriate to use the area of

TABLE I. Summary of the test conditions at a single SWJ actuator position.

Test case	P1-U7.4	P1-U15.1	P1-U25.1	P2-U7.4	P2-U15.1	P2-U25.1
Actuator streamwise position (x)	$-0.9D$ $(-0.8\delta_{\text{avg}})$	$-0.9D$ $(-0.8\delta_{\text{avg}})$	$-0.9D$ $(-0.8\delta_{\text{avg}})$	$-3.9D$ $(-3.7\delta_{\text{avg}})$	$-3.9D$ $(-3.7\delta_{\text{avg}})$	$-3.9D$ $(-3.7\delta_{\text{avg}})$
U_{jet} (m/s)	7.3					
U_{ref} (m/s)	7.4	15.1	25.1	7.4	15.1	25.1
VR	1	0.5	0.3	1	0.5	0.3
St_{jet}	0.018					
C_μ^* (%)	1.3	0.4	0.1	1.3	0.4	0.1
$\text{Re}(\times 10^4)$	1.2	2.5	4.1	1.2	2.5	4.1

the uncontrolled separation bubble in which the sweeping jet actuator is supposed to provide flow control. This allows the momentum coefficient to be more representative of the overall control effectiveness of the sweeping jet actuator. The area was obtained by taking the product of the reattachment length and six hydraulic diameters (PIV data are available to show that there is positive control effect for this spanwise range). As compared to Koklu [19] whereby the planform area was much larger and included surface areas without the separation bubble, the computation method of S here will lead to slightly larger momentum coefficients.

In addition, for the A_n term in Eq. (4), it is better to use the area at the nozzle throat instead of the area at the nozzle exit. The reasons are similar to those stated in Koklu [19], where the momentum coefficient was also computed based on the nozzle throat area. First, the sweeping motion of the jet means that the flow does not fully fill the entire divergent part of the nozzle. As such, it is not meaningful to use the nozzle exit area to calculate the momentum coefficient. For the very same reason, the throat velocity was used to compute the velocity ratio in Eq. (2). Second, the nozzle exit area is dependent on the opening, skew, and pitch angles, of which the latter two change with the mounting configuration of the SWJ actuator. In contrast, the nozzle throat area is independent of the mounting configurations and will allow the momentum coefficient to represent the current flow scenario more accurately. The revised momentum coefficient based on the nozzle throat area and approximated separation bubble area can be expressed as

$$C_\mu^* = \frac{D}{3(L)}(\text{VR})^2, \tag{5}$$

where L represents the reattachment length.

A summary of the test conditions associated with the six different test cases (three reference velocities and two actuator positions) is provided in Table I. The test cases are abbreviated based on the position of the actuators and the reference velocity as shown in the first row of Table I. For example, P1-U7.4 represents an actuator positioned at $0.9D$ upstream of the separating edge with a reference velocity of $U_{\text{ref}} = 7.4\,\text{m/s}$, while P2-U25.1 represents an actuator positioned at $3.9D$ upstream of the separating edge and with a reference velocity of $U_{\text{ref}} = 25.1\,\text{m/s}$. For the sake of brevity, the test cases with flow control will be referred to by their abbreviated names in the subsequent sections of this study.

III. RESULTS AND DISCUSSIONS

A. Ensemble-averaged streamwise 2D-2C velocity and the separation bubble

1. Baseline ramp flow

The velocity contours of the baseline ramp flow (without flow control) normalized by the reference velocity (U_{ref}) and ramp height (H) are presented in Figs. 4(a) (i), 4(b) (i), and 4(c) (i). The

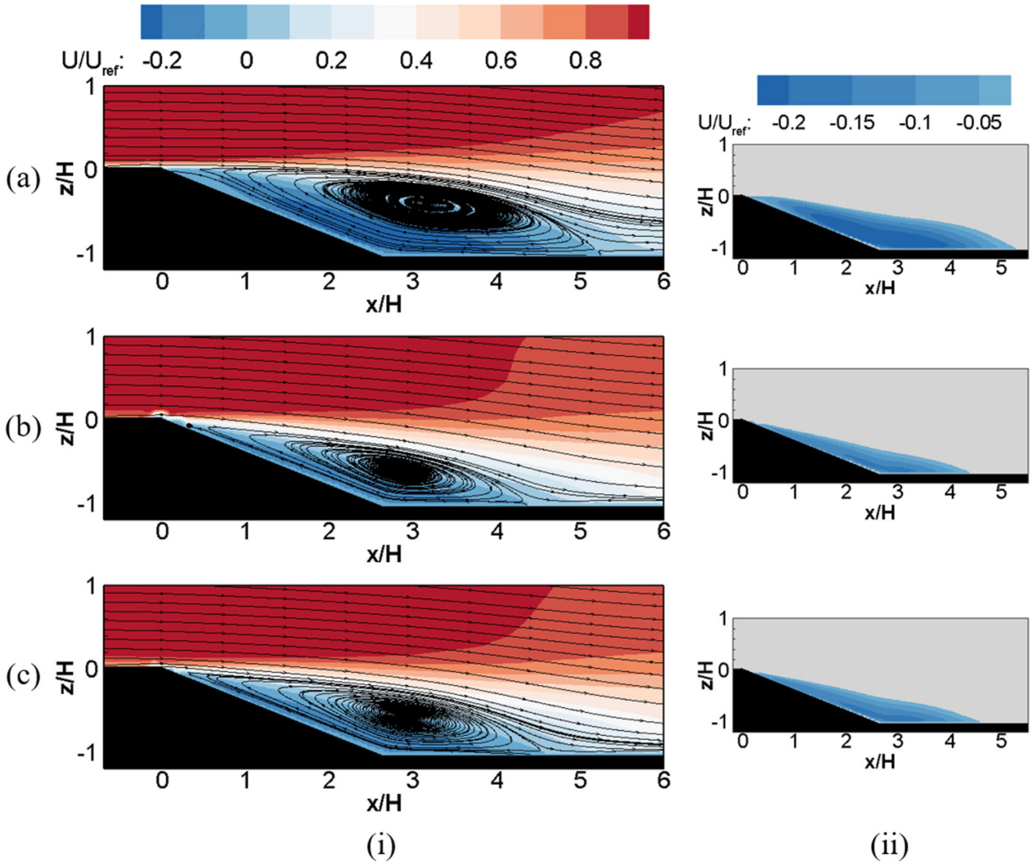

FIG. 4. Baseline ramp flow at $y/D = 0$ measurement plane for (a) $U_{\text{ref}} = 7.4\,\text{m/s}$, (b) $U_{\text{ref}} = 15.1\,\text{m/s}$, and (c) $U_{\text{ref}} = 25.1\,\text{m/s}$. (i) Ensemble-averaged velocity contours with superimposed streamlines and (ii) the separation bubble.

boundary layer just upstream of the separating edge can be characterized by the shape factor using the velocity profiles extracted at $x/H = -0.5$. The shape factor of the boundary layer is defined as

$$H_{\text{BL}} = \frac{\delta^*}{\theta}, \tag{6}$$

where δ^* and θ represents the displacement and momentum thickness respectively. The shape factor associated with the $U_{\text{ref}} = 7.4\,\text{m/s}$ test case was $H_{\text{BL}} = 2.16$, and the shape factors associated with the $U_{\text{ref}} = 15.1\,\text{m/s}$ and $U_{\text{ref}} = 25.1\,\text{m/s}$ test cases were both $H_{\text{BL}} = 1.44$. For boundary layers associated with flow along a flat plate, the shape factor of the Blasius boundary layer is $H_{\text{BL}} = 2.6$, while turbulent boundary layers are typically around $H_{\text{BL}} = 1.4$. As such, the boundary layer flow upstream of the separating edge is likely to be transitional for the $U_{\text{ref}} = 7.4\,\text{m/s}$ test case, and turbulent for the $U_{\text{ref}} = 15.1\,\text{m/s}$ and $U_{\text{ref}} = 25.1\,\text{m/s}$ test cases.

The flow created by the ramp was only an approximation of, and not the same as, the flow along a flat plate. Hence, the type of boundary layer was further assessed using HWA measurements. A hot-wire probe was inserted into the boundary layers of all three test cases at the approximate location of $z = 1.5$ mm and $x/H = -0.56$. The wind tunnel was then operated at a very low velocity for the first 10 s (approximately <2 m/s) to obtain a laminar boundary layer as reference. Thereafter, it was gradually adjusted to one of the three reference velocities of $U_{\text{ref}} = 7.4$, 15.1, and 25.1 m/s

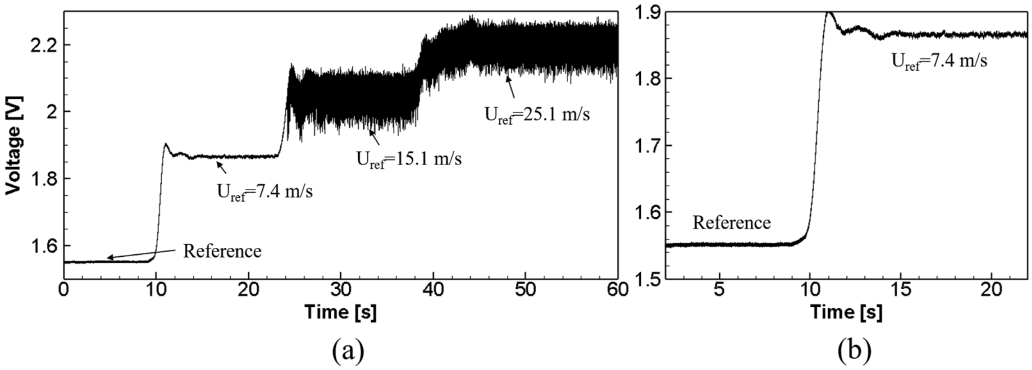

FIG. 5. Qualitative characterization of the boundary layer using a single continuous HWA measurement. (a) Measured voltage signals for the entire acquisition time and (b) magnified view of the reference and $U_{\mathrm{ref}} = 7.4\,\mathrm{m/s}$ test cases.

after approximately every 15 s. The measured voltage signals, sampled at a frequency of 5 kHz and in a single continuous recording, are presented in Fig. 5(a). Figure 5(b) shows the magnified view of the voltage signals for the reference and $U_{\mathrm{ref}} = 7.4$ m/s test cases.

From the voltage signals, it is immediately clear that the fluctuations were much higher for the $U_{\mathrm{ref}} = 15.1$ and 25.1 m/s test cases as compared to the reference and $U_{\mathrm{ref}} = 7.4\,\mathrm{m/s}$ test cases. This result along with the shape factors ($H_{\mathrm{BL}} = 1.44$) obtained from the PIV measurements indicate that the boundary layers associated with the $U_{\mathrm{ref}} = 15.1$ and 25.1 m/s test cases are turbulent. For the $U_{\mathrm{ref}} = 7.4\,\mathrm{m/s}$ test case, although the voltage signal appeared to be very similar to that of the reference laminar boundary layer, the magnified view shown in Fig. 5(b) indicates a slightly noisier signal with higher fluctuations. This suggests a transitional-laminar boundary layer, which agreed well with the shape factor ($H_{\mathrm{BL}} = 2.16$) obtained from PIV measurements.

Figures 4(a) (i), 4(b) (i), and 4(c) (i) show the streamlines superimposed on the ensemble-averaged velocity contours for the three reference velocities, while Figs. 4(a) (ii), 4(b) (ii), and 4(c) (ii) show the corresponding reverse flow region that is representative of the separation bubble, at the $y/D = 0$ measurement plane. The largest separation bubble was observed in the $U_{\mathrm{ref}} = 7.4\,\mathrm{m/s}$ test case [see Fig. 4(a)] and had a reattachment length of $x/H = 5.3$. In contrast, the separation bubbles in the $U_{\mathrm{ref}} = 15.1\,\mathrm{m/s}$ and $U_{\mathrm{ref}} = 25.1\,\mathrm{m/s}$ test cases were much smaller, but similar in size between themselves with reattachment lengths of $x/H = 4.4$ and 4.6 respectively. Although flow separation and reversal occurs due to adverse pressure gradient, a past study has shown that the pressure gradient is unlikely to have a significant role in influencing the size of the separation bubble and reattachment positions [32].

The differences in the size of the separation bubble (particularly for the $U_{\mathrm{ref}} = 7.4\,\mathrm{m/s}$ test case) are more likely to be due to the type of boundary layer before flow separation occurs. A transitional-laminar boundary layer is less energetic than a turbulent boundary layer, hence the separation bubble and reattachment length are expected to be larger, and this was observed in the current study. For the same reason, many flow separation control strategies (such as vortex generators, blowing, and suction) usually involve reenergizing the boundary layer to reduce or eliminate the separation bubble. Minor differences between the $U_{\mathrm{ref}} = 15.1\,\mathrm{m/s}$ and $U_{\mathrm{ref}} = 25.1\,\mathrm{m/s}$ test cases also show that an increase in the Reynolds number did not have as significant an effect on the separating flow as compared to the type of the boundary layer before separation.

2. *SWJ actuator at P1 ($x/D = -0.9$ or $x/\delta_{\mathrm{avg}} = -0.8$)*

When the sweeping jet actuator was introduced at the streamwise position P1 ($x/D = -0.9$), there was a very significant reduction in the size of the separation bubble for all three wind tunnel

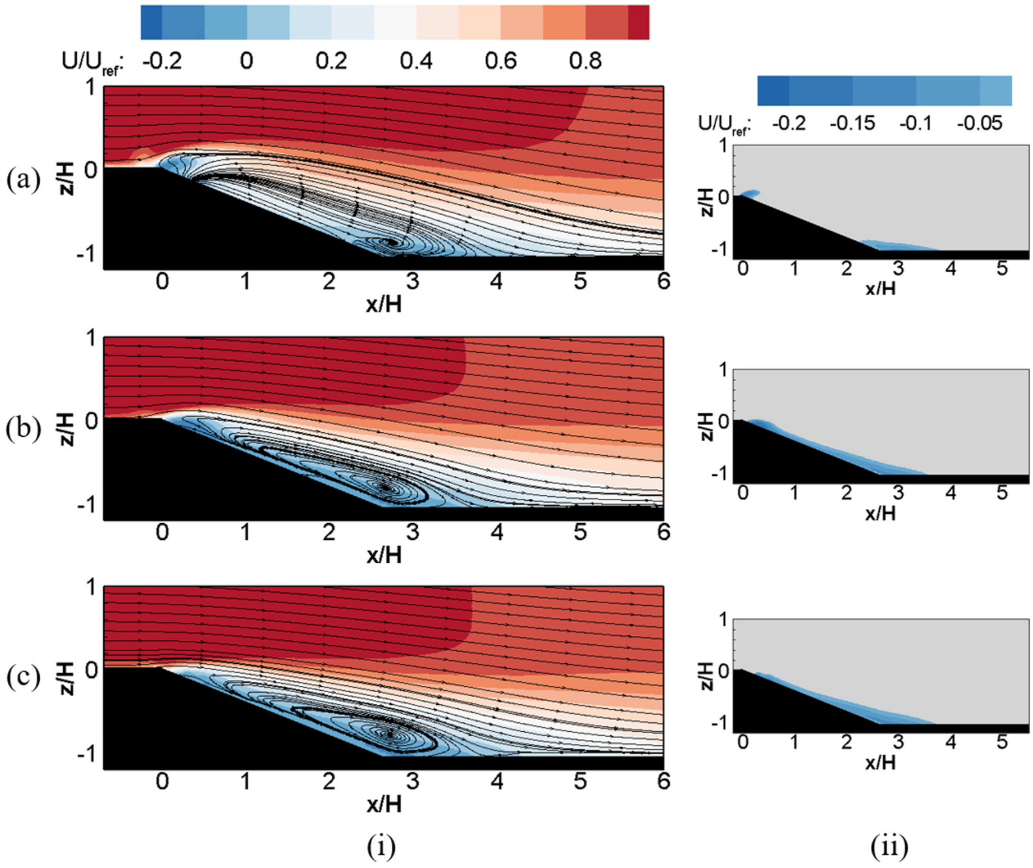

FIG. 6. Ramp flow with control at the $y/D = 0$ measurement plane for (a) P1-U7.4 (VR = 1), (b) P1-U15.1 (VR = 0.5), and (c) P1-U25.1 (VR = 0.3) test cases. (i) Ensemble-averaged velocity contours with superimposed streamlines and (ii) the separation bubble.

reference velocities of $U_{\mathrm{ref}} = 7.4$, 15.1, and 25.1 m/s, as shown in Figs. 6(a)–6(c) respectively. Among the three test cases, the $U_{\mathrm{ref}} = 7.4\,\mathrm{m/s}$ test case which had the largest separation bubble without flow control now displayed the smallest separation bubble [see Fig. 6(a) (ii)]. Its reattachment length has also decreased from $x/H = 5.3$ to $x/H = 3.8$. This result made sense because the flow control was applied to a transitional-laminar boundary layer that was expected to be more receptive than a turbulent boundary layer. Furthermore, the velocity ratio and momentum coefficient were the greatest here, at VR = 1 and $C_\mu^* = 1.3\%$ respectively.

Interestingly, there was an additional flow separation region near the separating edge, which occurred only for the P1-U7.4 test case, as shown in Fig. 6(a). This separation bubble was located close to the origin and was much smaller than the primary separation bubble at the base of the ramp. Its occurrence can be attributed to the sweeping jet injecting into the crossflow at high VR, which represents a deeper intrusion of the jet into the crossflow during all phases of the sweeping jet's oscillation cycle, as well as the formation of a localized low-pressure region immediately downstream of the jet injection. Coupled with the sudden sharp change in ramp geometry which leads to a sudden increase in the adverse pressure gradient [18,39,40], early flow reversal occurred, and this led to the formation of the secondary separation bubble observed directly downstream of the jet injection position.

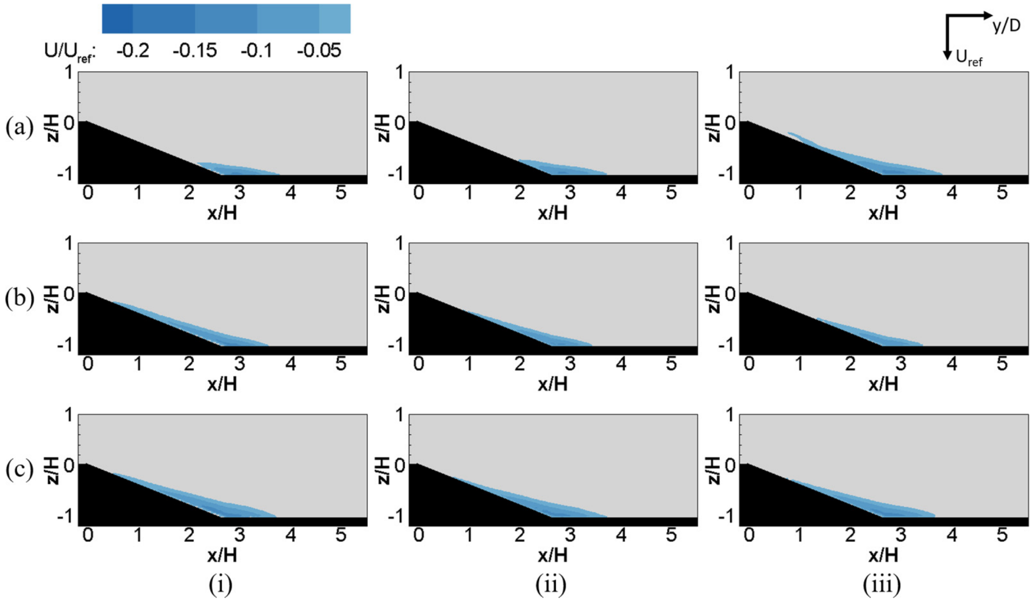

FIG. 7. The separation bubble at (a) P1-U7.4, (b) P1-U15.1, and (c) P1-U25.1 test cases. Measurement planes at (i) $y/D = 1$, (ii) $y/D = 2$, and (iii) $y/D = 3$.

The *xz* plane of the separation bubble measured at the locations $y/D = 1$, 2, and 3 are presented in Fig. 7(a) for the P1-U7.4 test case. For all three measurement planes, positive flow control effects can be observed based on a reduction in the size of the separation bubbles relative to the baseline. The sizes of the separation bubbles were all very similar in the three measurement planes but can still be observed to increase slightly as the measurement plane progresses away from $y/D = 0$. This result was not reflected in the ensemble-averaged nondimensional reattachment length shown in Fig. 8(a), which was very similar (around $x/H = 3.7$–3.8) across all measurement planes.

Evidently, the reattachment length can only be used as a rough indication of flow separation control performance, as it is a one-dimensional (1D) parameter that does not contain information on the actual size (height) of the separation bubble and changes to its 3D geometry. The height (and consequently volume) of the separation bubble is important as it is an indication on the amount of additional energy required to be added to the flow (through flow control devices) in order to eliminate the separation bubble. For two separation bubbles of the same length, the one with larger height is expected to require higher levels of momentum transfer and entrainment in order to eliminate the separation bubble. The height of the recirculation region is also of importance in other applications, which includes urban air pollution studies, where the size of the recirculation zone on the leeward side of buildings can have significant impacts on the local pollutant concentration, and engine intake design studies, where minimizing the total pressure losses of the flow is of interest.

In order to circumvent the limitations of the reattachment length, and allow for meaningful quantitative evaluation on the size reduction of the separation bubble based on the available 2D PIV data, the cross-sectional (*xz* plane) areas of the separation bubble, normalized by the original area of the uncontrolled separation bubble at $y/D = 0$, are presented in Fig. 8(b). The choice of the normalization parameter allows Fig. 8(b) to characterize the flow separation control performance at various wind tunnel reference velocities, actuator positions, and measurement planes, relative to the baseline previously presented in Fig. 4. Based on Fig. 8(b), it is now clear that for the P1-U7.4 test case, the size of the separation bubble increases nonlinearly as the measurement plane shifts further away from $y/D = 0$. The $y/D = 0$ measurement plane remains an exception to this trend, due to

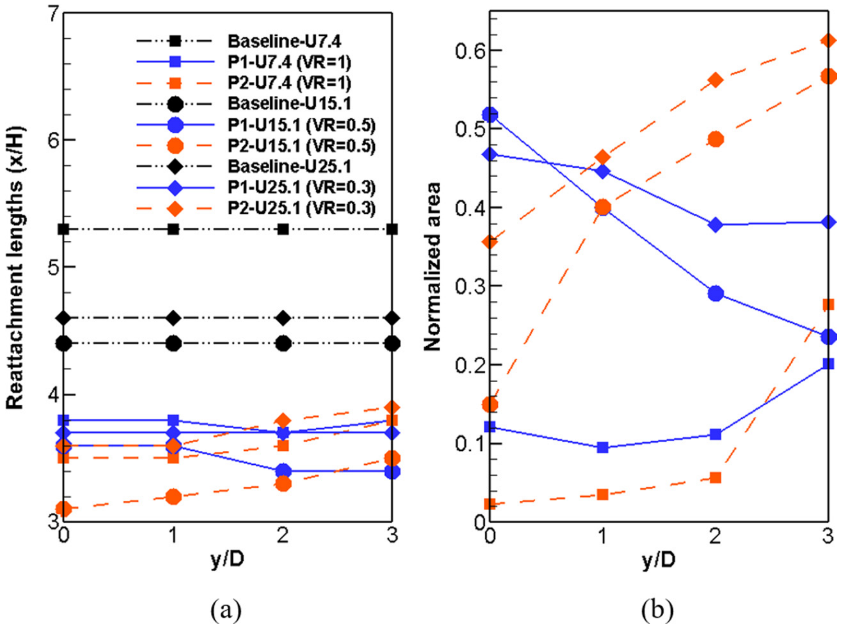

FIG. 8. (a) Time-averaged nondimensional reattachment lengths (x/H) and (b) cross-sectional (xz plane) normalized area of the separation bubble.

the formation of the secondary separation bubble which contributes to the overall area of the reverse flow region.

For the P1-U15.1 and P1-U25.1 test cases as shown in Figs. 6(b) and 6(c), the separation bubble in the $y/D = 0$ measurement plane can be observed to have decreased in size (relative to baseline) with the application of flow control. This is reaffirmed by the normalized area presented in Fig. 8(b), which is below 1 for both test cases. The reattachment lengths have also decreased from $x/H = 4.4$ to 3.6 and $x/H = 4.6$ to 3.7 respectively [see Fig. 8(a)]. Despite differences in the velocity ratio (momentum coefficient) and Reynolds number, the actual size of the separation bubbles for the two test cases appears to be comparable, as shown in Figs. 6(b) and 6(c).

In addition, the intrusion of the jet into the crossflow was small for these two test cases since the velocity ratios were smaller than that of the P1-U7.4 test case. With decreasing velocity ratio and momentum coefficient, the overshoot (upward trajectory) of the streamlines just before the separating edge decreases, and there was almost no overshoot that can be observed for the P1-U25.1 test case where VR = 0.3. No secondary separation bubble was observed near the separating edge for these two test cases even though a slight overshoot can still be observed in the P1-U15.1 test case. Positive flow control effects were also observed at the $y/D = 1$, 2, and 3 measurement planes of the P1-U15.1 and P1-U25.1 test cases as shown in Figs. 7(b) and 7(c) respectively. With an increase in y/D, the size of the separation bubble decreases very slightly for both test cases [see Fig. 8(b)].

3. SWJ actuator at P2 ($x/D = -3.9$ or $x/\delta_{avg} = -3.7$)

The $y/D = 0$ velocity contours associated with the SWJ actuator at location P2 ($x/D = -3.9$) are presented in Fig. 9. As compared to the results shown in Fig. 6, the separation bubbles of all three test cases here appeared to be even smaller and had shorter reattachment lengths than their counterparts at the same reference velocities. In fact, the separation bubble was almost eliminated completely for the P2-U7.4 test case as shown in Fig. 9(a) (ii), with a bubble normalized area of only 0.023 [see Fig. 8(b)]. This result showed that implementing the actuators at P2 (instead of P1) was able to provide better flow separation control for all three wind tunnel reference velocities in the

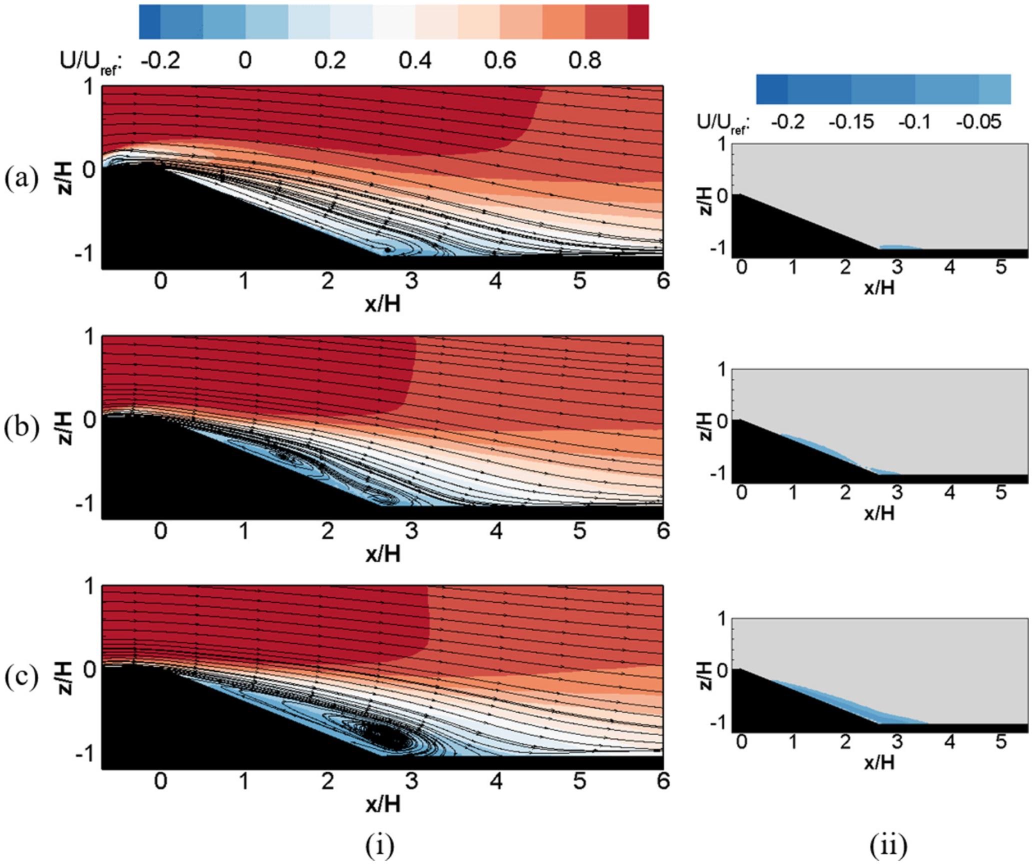

FIG. 9. Ramp flow with control at the $y/D = 0$ measurement plane for (a) P2-U7.4 (VR = 1), (b) P2-U15.1 (VR = 0.5), and (c) P2-U25.1 (VR = 0.3) test cases. (i) Ensemble-averaged velocity contours with superimposed streamlines and (ii) the separation bubble.

$y/D = 0$ measurement plane. The result is perhaps surprising and unexpected, as past studies have shown that actuators nearer to the onset of separation tend to perform better in terms of separation control. For example, for flow separation control of a Stratford ramp, SWJ actuators performed better when located at 2.3δ (versus 7δ) upstream of the onset of flow separation [19]. Nevertheless, there are three main differences in the current study as compared to that of the Stratford ramp by Koklu [19], which could have led to the contrasting observations.

First, most of the test cases investigated by Koklu [19] made use of surface pressure measurements and surface oil flow visualization. These are experimental techniques that are unable to reveal the reverse flow region in the vertical direction (z direction) away from the surfaces. In contrast, the current study has presented results of the 2D PIV technique at multiple y/D locations, which is much more suitable for the study of variations in the 3D geometry of the separation bubble. Second, the minimal distance of the SWJ actuator to the separating edge in the current study was approximately $0.8\delta_{\text{avg}}$ ($x/D = -0.9$ location), which was much closer to the separating flow than what was investigated by Koklu [19] (the minimal distance was 2.3δ). Third, the ramp model in the current study featured a sharp change in geometry as compared to a smooth geometrical variation in the Stratford ramp. This is likely to represent a sharper increase in the adverse pressure gradient. It is possible that below a certain critical distance, estimated by the authors to be below one boundary layer thickness, the region of low pressure produced by the jet in crossflow coincides with the position where the separating flow starts to occur (at the separating edge). The sharp change in ramp geometry further exacerbates the adverse pressure gradient experienced by the flow. As a result, although the boundary layer was reenergized by the sweeping jet, it was counteracted by a stronger local adverse pressure gradient, which led to a poorer control effect for all three wind tunnel reference velocities as compared to actuators located slightly further upstream at P2 ($x/D = -3.9$).

Another important observation can be made based on the P2-U7.4 test case as shown in Fig. 9(a). Although the streamwise velocity just downstream of the actuator was very close to zero, there was no reverse flow, and a secondary separation bubble was not observed. Since a secondary separation bubble was observed only in the P1-U7.4 test case, it appears that there are two necessary conditions for the secondary separation bubble to form. First, the velocity ratio must be sufficiently high for the jet to intrude significantly into the main flow ($\mathrm{VR} > 1$) to create a region of low pressure immediately downstream of the jet. Second, the SWJ actuator has to be located sufficiently close to and upstream of the separating edge such that the adverse pressure gradient induced by the sharp change in ramp geometry is able to interact with the low pressure region created by the jet, to induce the formation of the secondary separation bubble. Although the formation of the additional secondary separation bubble was undesirable, simply avoiding its formation is unlikely to improve the control effect either, since the size of the primary separation bubble in the $y/D = 0$ measurement plane was also smaller for the P2-U15.1 and P2-U25.1 test cases (no secondary separation bubble was observed) as compared to the P1-U15.1 and P1-U25.1 test cases.

When comparing the P2-U7.4, P2-U15.1, and P2-U25.1 test cases in the $y/D = 0$ measurement plane (see Fig. 9), it can be observed that the size of the separation bubble was the smallest for the P2-U7.4 test case, and the largest for the P2-U25.1 test case. Relative to their respective baseline separation bubble, the P2-U7.4, P2-U15, and P2-U25.1 test cases had a normalized area of 0.023, 0.15, and 0.357 respectively [see Fig. 8(b)]. This indicates that for a fixed supply rate of the SWJ actuator, the flow separation control effect was more effective at lower wind tunnel reference velocities. In fact, this also holds true for the $y/D = 1$, $y/D = 2$, and $y/D = 3$ measurement planes as shown in Fig. 8(b) previously. This result is within reasonable expectations, since the P2-U7.4 test case has a transitional-laminar boundary layer as explained earlier, and the flow is expected to be the most receptive to flow control strategies. In addition, the momentum coefficient of the P2-U7.4 test case ($C_\mu^* = 1.3$) was also a lot higher than the P2-U15.1 and P2-U25.1 test cases ($C_\mu^* = 0.4$ and 0.1 respectively). For the P2-U15.1 and P2-U25.1 test cases where both had turbulent boundary layers before the separation occurred, more effective flow control of the P2-U15.1 test case (vs P2-U25.1 test case) can be attributed to a higher momentum coefficient. Note that the type of boundary layer is likely to play a more important role than the momentum coefficient in determining the effectiveness of flow control, as differences in the size of the separation bubble between the P2-U15.1 and P2-U25.1 test cases were relatively smaller.

The results associated with measurement planes $y/D = 1$, 2, and 3 for all three reference velocities are shown in Fig. 10. As compared to the baseline test case (without flow control), the separation bubble has decreased in size for all test cases here, which is indicative of the flow control effectiveness of the SWJ actuator for the entire spanwise measurement range. It can also be observed that the size of the separation bubble increases as y/D increases from $y/D = 0$ to $y/D = 3$ for all three test cases [see Figs. 8(b) and 10]. This observation differed from the P1-U15.1 and P1-U25.1 test cases which showed an opposing trend.

The trends are different for the two actuator positions (P1 and P2) because the optimal actuator position changes for different measurement planes. Table II summarizes the optimal actuator position from the perspective of the measurement planes. At the $y/D = 0$ measurement plane, the SWJ actuator at position P1 performed poorer than P2 for all three reference velocities, and this has been discussed earlier and was attributed to the coincidence of the low-pressure region created by the jet in crossflow and the adverse pressure gradient induced by the sudden change in ramp geometry.

As the measurement planes deviated further from the $y/D = 0$ measurement plane, the SWJ actuator performed better when positioned at P1 instead of P2. This can be attributed to stronger

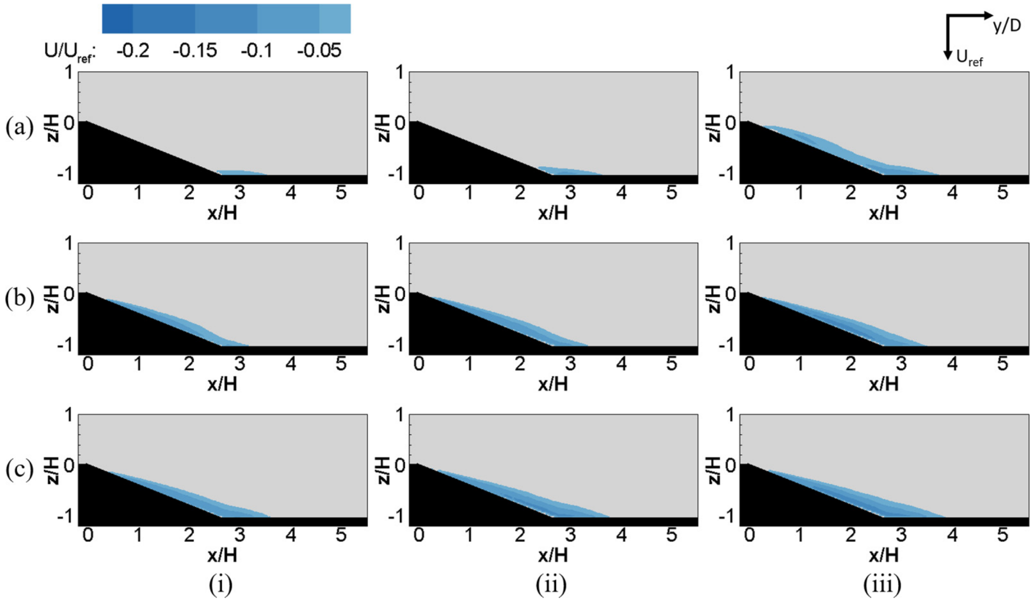

FIG. 10. The separation bubble at (a) P2-U7.4, (b) P2-U15.1, and (c) P2-U25.1 test cases. Measurement planes at (i) $y/D = 1$, (ii) $y/D = 2$, and (iii) $y/D = 3$.

vortices with minimal decay in vortex strength as evidenced in an earlier study [19], and the localization of the low-pressure region created by the jet in crossflow, which is estimated to be approximately $-0.5 < y/D < 0.5$ based on the jet width of typical jet flows [34]. Hence, the detrimental effects of the low-pressure region are likely to be localized to measurement planes close to $y/D = 0$, while stronger flow vortices contributed to flow control of the separation bubble further from the $y/D = 0$ measurement plane.

B. Ensemble-averaged cross-stream 2D-3C velocity fields

1. *Spatial influence of the SWJ actuator*

The oscillatory motion of the sweeping jet is expected to produce flow control over a larger area in the spanwise direction as compared to a steady jet. As a result, the injection of streamwise vorticity and the low-pressure region created by the jet may affect a wider spanwise and vertical range than expected. Hence, it is necessary to better understand the effects of the actuator position based on the cross-stream velocity contours. Figure 11 shows the cross-stream (yz-measurement plane) stereoscopic PIV results captured at the location of $x/H = 0.2$. Note that the velocity vectors are presented at reduced resolution to avoid data clutter.

TABLE II. Optimal SWJ actuator position based on the cross-sectional (xz-plane) area ratio of the separation bubble.

Reference velocities	$y/D = 0$	$y/D = 1$	$y/D = 2$	$y/D = 3$
$U_{\text{ref}} = 7.4\,\text{m/s}$	P2	P2	P2	P1
$U_{\text{ref}} = 15.1\,\text{m/s}$	P2	similar	P1	P1
$U_{\text{ref}} = 25.1\,\text{m/s}$	P2	similar	P1	P1

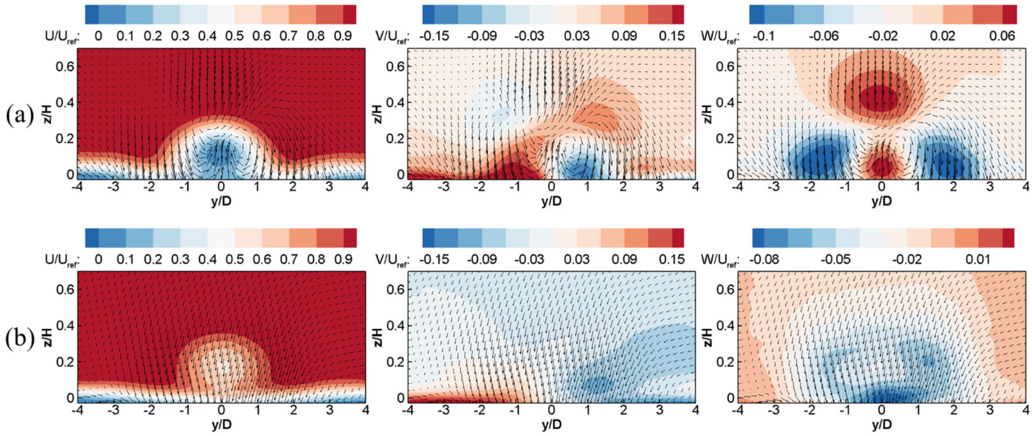

(i) (ii) (iii)

FIG. 11. Effect of SWJ actuator streamwise position on $x/H = 0.2$ measurement plane for (a) P1-U7.4 and (b) P2-U7.4 test cases. Nondimensional velocity contours for (i) streamwise, (ii) spanwise, and (iii) vertical velocity components.

When the SWJ actuator was positioned at P1 (instead of P2), the magnitude of the streamwise flow velocity can be observed to be much lower in the region near to the jet centerline at around $y/D = 0$ and $z/H = 0.1$, and close to the wall at around $z/H < 0$ [see Figs. 11(a) (i) and 11(b) (i)]. This indicates that the flow energy is lower near the $y/D = 0$ measurement plane. In addition, there is an upwash effect near the $y/D = 0$ plane as shown in Fig. 11(a) (iii), which redirects high momentum fluid away from the wall and further contributes to the weaker flow control effect of the SWJ actuator at P1.

For measurement planes far from $y/D = 0$, the streamwise velocities are comparable for the SWJ actuator at both P1 and P2 positions. This indicates that the low-pressure region created by the jet in crossflow is localized, and likely to be the cause of the lower streamwise velocities near the $y/D = 0$ plane. Figures 11(a) (iii) and 11(b) (iii) show the downwash created by the streamwise vortices generated by the sweeping jet, which appeared to be stronger for the $y/D = 2$ and 3 measurement planes when the SWJ actuator was positioned at P1. This is likely to play an important role in the improved performance of the SWJ actuator at P1 for the $y/D = 3$ plane.

The spatial influence of the SWJ actuator on the flow field also appeared to be much wider in the spanwise y direction when the actuator was positioned at P1. This is likely because significant mixing of jet with the ambient fluid and decay of vortical structures have already occurred at the $x/H = 0.2$ location if the SWJ actuator was positioned further upstream at P2 ($x/H = -3.9$) instead. The spanwise and vertical velocity contours shown in Figs. 11(a) (ii), 11(b) (ii), 11(a) (iii), and 11(b) (iii) support this reasoning, since the velocity components are much weaker and the flow structures are no longer well ordered when the SWJ actuator was positioned at P2 instead of P1. For the vertical z direction, the location corresponding to the lowest streamwise velocity was higher when the SWJ actuator was located at P2 (approximately $z/H = 0.17$) as compared to P1 (approximately $z/H = 0.11$). This can be attributed to the upward trajectory of the jet, which had a longer streamwise distance to develop upwards when the SWJ actuator was located further upstream at position P2.

The ensemble-averaged streamwise vorticity contour plots are presented in Fig. 12. The vorticity near the jet centerline can be clearly observed in the P1-U7.4 test case [see Fig. 12(a)] but not in the P2-U7.4 test case [see Fig. 12(b)]. This supports the earlier explanation of stronger decay of vortical structures when the SWJ actuator was positioned further upstream at position P2. Hence, the extent of spatial influence of the SWJ actuator on the flow field is highly dependent on its streamwise

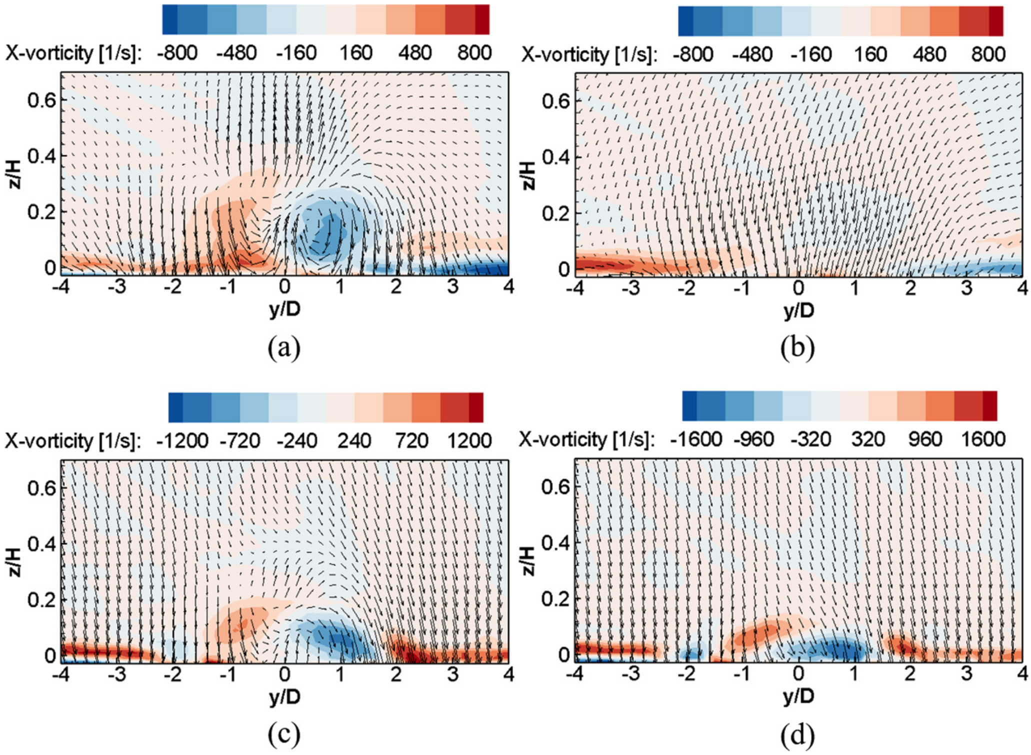

FIG. 12. Ensemble-averaged streamwise vorticity contours in the $x/H = 0.2$ measurement plane for (a) P1-U7.4 (VR = 1) (b) P2-U7.4 (VR = 1), (c) P1-U15.1 (VR = 0.5), and (d) P1-U25.1 (VR = 0.3) test cases.

location. The nearer the SWJ actuator is to the separating flow, the higher the velocity components are likely to be since significant jet mixing has not occurred and streamwise vortices are less likely to decay. As a result, this allows higher energy injection into the boundary layers that are further away from the $y/D = 0$ measurement plane. At the same time, the low-pressure region near the $y/D = 0$ measurement plane is likely to be wider and located lower, resulting in a larger localized low velocity region that is more likely to undergo flow reversal.

2. *Velocity ratio effects*

Next, the influence of the VR on the cross-stream flow field is examined. Figures 11(a), 13(a), and 13(b) present the effects of the VR on the flow field for VR = 1, 0.5, and 0.3 respectively. From the streamwise velocity contours, the overshoot of the jet into the main flow can be confirmed to be lower as the VR decreases, consistent with the 2D PIV results presented earlier. There appears to be little difference in the decay of the vortical structures as changes in VR did not significantly disrupt the flow structures, although they did appear to be flattened towards the wall as the VR decreases. This can also be observed in the streamwise vorticity contour plots shown in Figs. 12(a), 12(c), and 12(d), where the vorticity near the jet centerline were observed to flatten progressively towards the wall. Note that the horizontal strip of vorticity very close to the wall is due to the no-slip condition. The strength of the streamwise vortices (based on the vorticity values) increases as VR decreases which was within reasonable expectations. The spanwise extent of the low streamwise velocity region appeared to be very similar across VR = 0.5 and 0.3, within the range of $-1 < y/D < 1$ [see Figs. 13(a) (i) and 13(b) (i)]. In contrast, this region was much smaller for the VR = 1 test case [see Fig. 11(a) (i)].

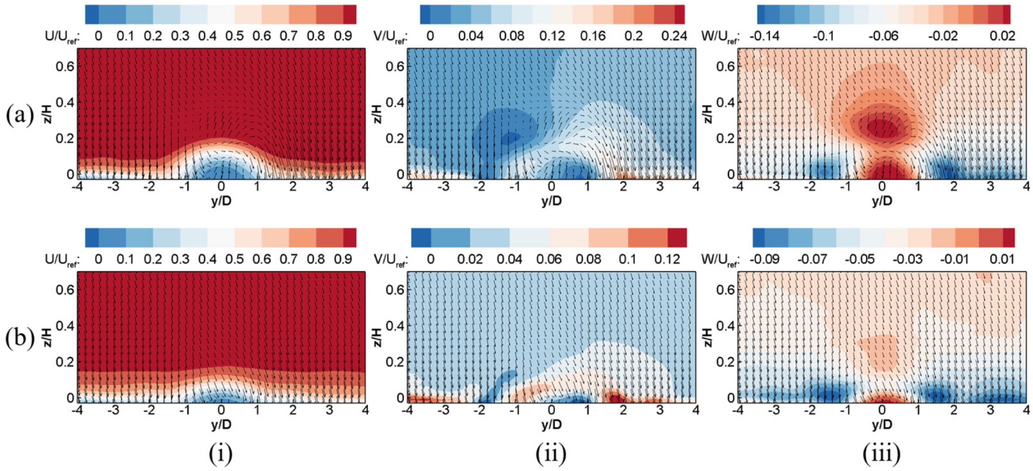

FIG. 13. Effect of VR on $x/H = 0.2$ measurement plane for (a) P1-U15.1 (VR = 0.5) and (b) P1-U25.1 (VR = 0.3) test cases. Nondimensional velocity contours for (i) streamwise, (ii) spanwise, and (iii) vertical velocity components.

C. Instantaneous cross-stream 2D-3C velocity fluctuations

1. *Upwash, downwash, and the formation of streamwise vortices*

The ensemble-averaged streamwise and cross-stream results have indicated that the actuator position has strong influences on the production of the secondary separation bubble in the P1-U7.4 test case. The underlying mechanism is examined by considering the instantaneous cross-stream velocity fluctuations at the $x/H = 0.2$ measurement plane for the P1-U7.4 test case, as shown in Fig. 14. Although these are instantaneous results, the flow features in most of the instantaneous snapshots were similar to those presented in either Figs. 14(a), 14(b), or 14(c). This is probably because the measurement plane was less than two jet diameters downstream of the SWJ actuator, hence it is highly likely that the periodic flow features produced by the SWJ actuator were not significantly disrupted when it advected downstream to the measurement plane. Three velocity fluctuations fields selected as representative velocity fields of the sweeping jet at different phases of the sweep cycle are presented in Fig. 14. Note that at any time instance, there is a phase lag between the actual phase of the sweep cycle and the measurements taken at the $x/H = 0.2$ plane, and the flow structures discussed in Fig. 14 were actually produced by the SWJ actuator at an earlier time that had advected downstream to the measurement plane.

When the jet swept to the right, the flow structures produced by the SWJ actuator advected less than two jet diameters downstream to the measurement plane, and a localized upwash effect created due to the upward momentum of the primary jet flow can be observed in Fig. 14(a) (i). Small rollups which are typical of jet flows can be observed on the shear layer at the right side of the jet and these are marked as Kelvin-Helmholtz (KH) instability as shown in Fig. 14(a) (iii). These rollups were not as clearly observed in Fig. 14(b) (iii) at around the $y/D = -1.5$ location due to several possible reasons such as limited vector resolution, small length scale of the structures, strong three-dimensionality effects, and that the measurement plane was not directly at the plane of the SWJ actuator. The region of strong upwash in Fig. 14(a) (i) coincides with the region that showed strong negative streamwise velocity shown in Fig. 14(a) (ii). Similar observations can also be made when the jet swept to the left [see Figs. 14(b) (i) and 14(b) (ii)] and the center positions [see Figs. 14(c) (i) and 14(c) (ii)], which proves that the production of the secondary separation bubble [previously shown in Fig. 6(a)] is strongly influenced by the localized upwash effect of the jet. The

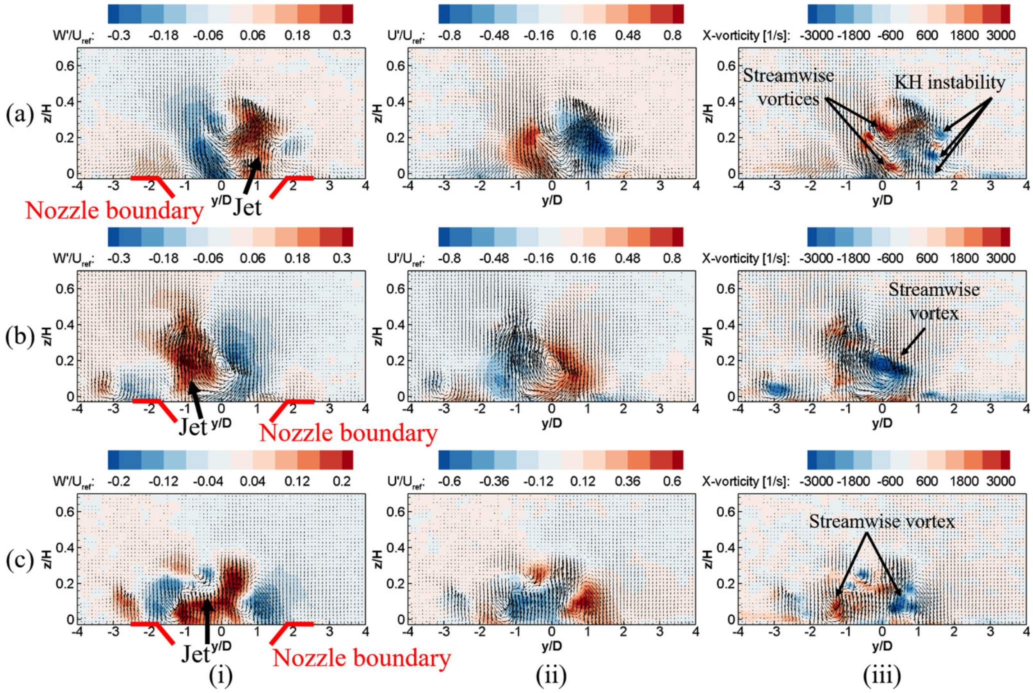

FIG. 14. Cross-stream results at $x/H = 0.2$ measurement plane for the P1-U7.4 test case. Sweeping jet directed to the (a) right, (b) left, and (c) center positions. Instantaneous nondimensional (i) vertical and (ii) streamwise velocity fluctuations contours, and (iii) instantaneous streamwise vorticity contours.

upwash produced by the jet is detrimental to flow control as it redirects high momentum ambient fluid away from the low momentum region near the wall.

To the left of the jet centerline in Fig. 14(a) (i), a strong downwash effect can be observed, and the magnitude of the downwash velocity fluctuations was similar to that of the upwash created by the jet flow. The downwash region is likely to be induced by the sweeping motion of the jet which displaces ambient fluid at the leading side of the jet and creates a negative pressure region at the trailing side of the jet. The region of strong downwash coincides with the region that showed strong positive streamwise velocity fluctuations in Fig. 14(a) (ii), and the same trend was also observed in both Figs. 14(b) and 14(c). This shows that the strong downwash region (bulk flow motion) is very effective at entraining high momentum ambient fluid into the low momentum region near the wall, leading to a localized region of strong positive streamwise velocity fluctuations that counteract flow separation. It is further noted that the regions of strong downwash and upwash at different phases of the sweep cycle overlapped each other as shown in Figs. 14(a) and 14(b), which explains why no secondary separation bubble was observed in the $y/D = 1$ measurement plane [see Fig. 7(a) (i)] of the ensemble-averaged streamwise velocity contours.

One of the very interesting flow features that can be observed in Fig. 14 is that the strong upwash and downwash regions had combined to form large-scale primary streamwise flow structures. In Fig. 14(b) (iii), the streamwise vortex was almost two jet diameters in length scale, and for Fig. 14(a) (iii), primary streamwise vortices induced by the strong upwash and downwash region appeared to form one on top of the other and with the same rotation signs. Streamwise flow structures can also be observed when the jet was near the center position [see Fig. 14(c) (iii)], although this occurred as a pair with opposite rotation signs and had a smaller length scale of approximately one jet diameter. These observations agreed well with the earlier work by Ostermann *et al.* [41], where it was shown that when the jet is at its maximum deflection, it interacts with the

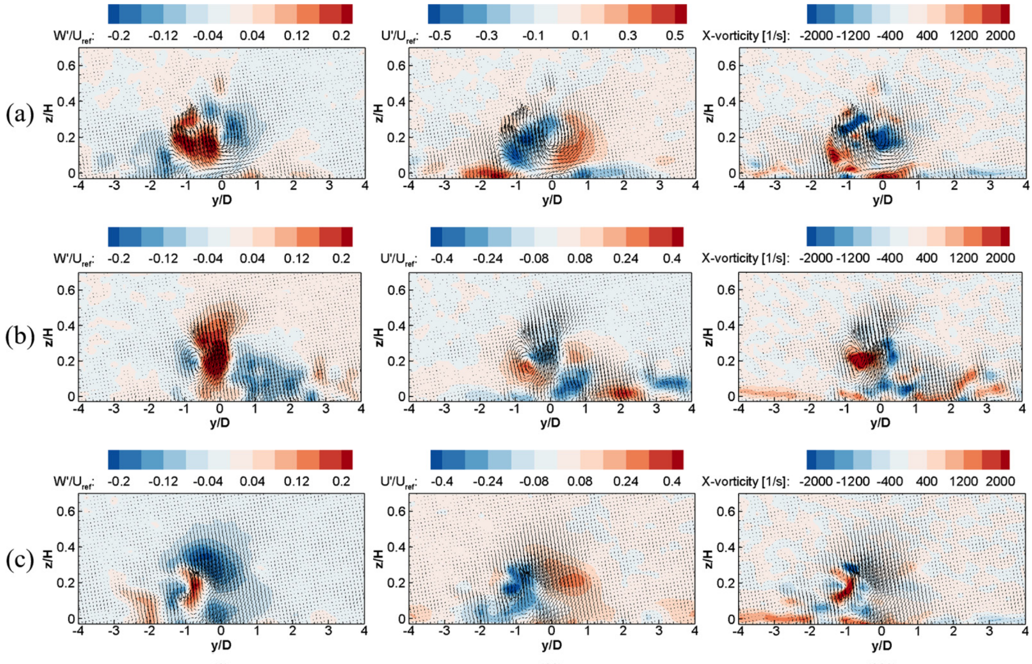

(i) (ii) (iii)

FIG. 15. Cross-stream results at $x/H = 0.2$ measurement plane for the P2-U7.4 test case. Arbitrary time instance (a) no. 1, (b) no. 2, and (c) no. 3. Instantaneous nondimensional (i) vertical and (ii) streamwise velocity fluctuations contours, and (iii) instantaneous streamwise vorticity contours.

crossflow to generate streamwise vortices, and when the jet is near the center position, a spanwise vortex connected to pairs of streamwise vortices is formed.

There were also instances where multiple streamwise flow structures of smaller length scales can be observed. These were generally observed to occur under two circumstantial events: (1) When the jet is near the center position and the downwash is relatively weaker at both sides of the upwash, there is a tendency to form either one [see Fig. 14(c)] or more than a pair of streamwise flow structures with opposite signs at either side of the upwash. (2) When the jet is away from the centerline and the downwash and upwash regions are far apart from each other, a splitting of a large-scale streamwise vortex [such as the one shown in Fig. 14(b) (iii)] in the vertical direction can occur, resulting in the formation of multiple streamwise flow structures stacked vertically and with the same rotation signs [see Fig. 14(a) (iii)].

2. Effects of the actuator position on the secondary separation bubble

In the P2-U7.4 test case, since the Reynolds number and velocity ratios were similar to the P1-U7.4 test case, the flow structures produced by the SWJ actuator are expected to be similar to those of the P1-U7.4 test case. However, one key difference is that there is now a larger streamwise distance between the SWJ actuator and the measurement plane. As such, regular flow patterns and vortices produced by the SWJ actuator are much more likely to have been disrupted by three-dimensional effects by the time they had advected to the measurement plane. Hence, it was difficult to find representative instantaneous velocity fluctuations that can describe the flow field at different phases of the sweep cycle for the P2-U7.4 test case. Nonetheless, certain important trends can still be observed in the instantaneous cross-stream velocity fluctuations, hence three selected velocity fluctuation fields are presented in Fig. 15.

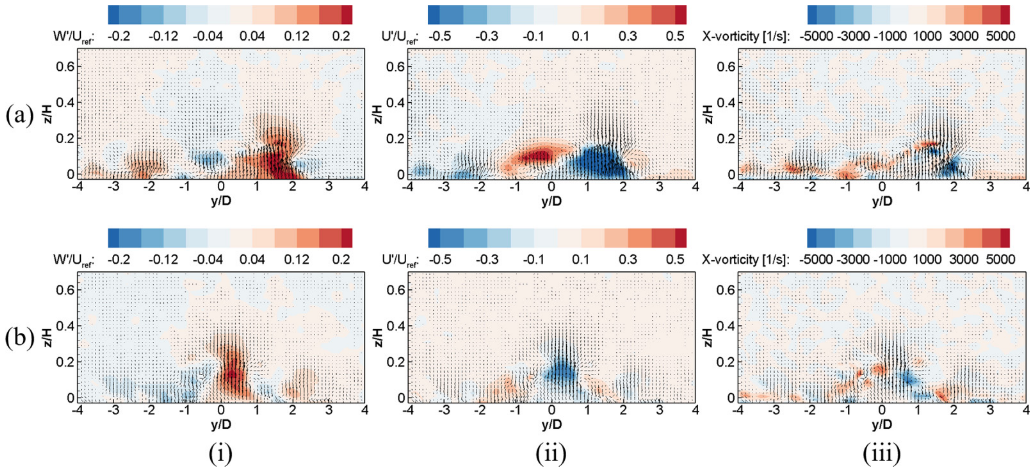

FIG. 16. Cross-stream results at $x/H = 0.2$ measurement plane for P1-U15.1 test case. Arbitrary time instance (a) no. 1, (b) no. 2, and (c) no. 3. Instantaneous nondimensional (i) vertical and (ii) streamwise velocity fluctuations contours, and (iii) instantaneous streamwise vorticity contours.

There were many instances where regions of strong upwash were observed to lift off the wall in the P2-U7.4 test case and this is shown in Figs. 15(a) (i), 15(b) (i), and 15(c) (i). This is as opposed to the P1-U7.4 test case where the strong upwash region was observed to be very close to the wall. The lifting of the upwash region is related to the slight upward trajectory of the flow field due to the jet flow injection, which can be verified by examining the velocity contours from Fig. 9(a), where streamlines were observed to be redirected upwards until around the start of the ramp at $x/H = 0$. The lifting of the upwash region had two consequences which greatly contributes to the mitigation of flow separation along the jet centerline plane. First, the region of strong upwash is no longer close to the wall where low momentum fluid resides. This reduces the probability of flow separation since the upwash region is linked to negative streamwise velocity fluctuations. Second, downwash and horizontal velocity fluctuations have entered the region close to the wall [see Figs. 15(a) and 15(c)]. These are likely to be secondary flow structures induced by the primary large-scale streamwise vortices, which then serve to entrain high momentum ambient fluid into the wall region, hence reenergizing the flow and mitigating flow separation.

It is noted that the strongest upwash regions can still be associated with negative streamwise velocity fluctuations as shown in Figs. 15(a) (ii), 15(b) (ii), and 15(c) (ii). Nonetheless, this is no longer particularly important as these regions are no longer located near the wall where low momentum fluid resides. In addition, regions of relatively weak upwash and downwash were observed to be weakly correlated with negative and positive streamwise velocity fluctuations respectively. As compared to the P1-U7.4 test case, the relationship between regions of upwash (downwash) and negative (positive) streamwise velocity fluctuations here appears to be weaker. The strong upwash and downwash regions created by the sweeping jet has also led to the formation of streamwise flow structures and this is shown in Figs. 15(a) (iii), 15(b) (iii), and 15(c) (iii). Much like the results of the P1-U7.4 test case previously presented in Fig. 14, the streamwise flow structures here can vary in distribution and length scale but were generally observed to be below one jet diameter for the latter.

3. *Velocity ratio effects*

The jet-to-reference velocity ratio (VR) effects on the flow field is revisited by examining the instantaneous cross-stream velocity fluctuation. Results of the P1-U15.1 and P1-U25.1 test cases measured at $x/H = 0.2$ measurement plane are presented in Figs. 16 and 17 respectively, while the P1-U7.4 test case has been presented in Fig. 14 previously. The flow patterns observed in both the

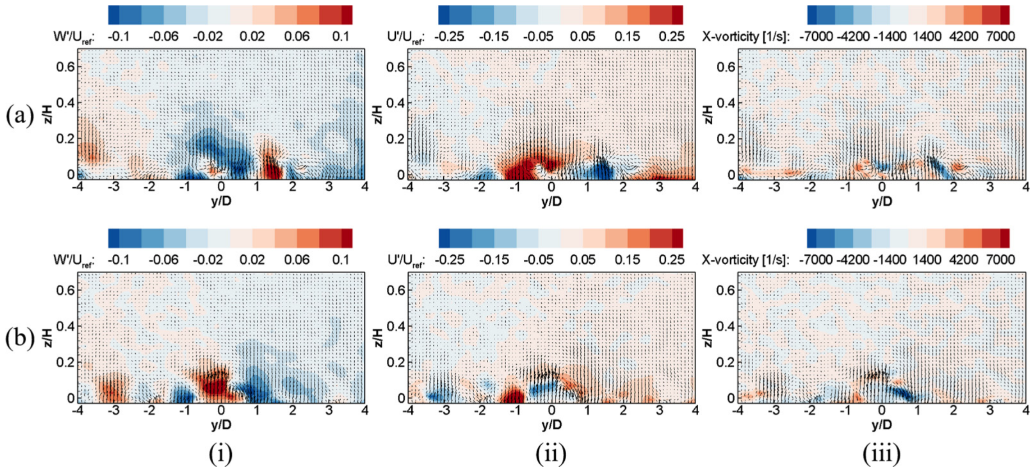

FIG. 17. Cross-stream results at $x/H = 0.2$ measurement plane for P1-U25.1 test case. Arbitrary time instance (a) no. 1, (b) no. 2, and (c) no. 3. Instantaneous nondimensional (i) vertical and (ii) streamwise velocity fluctuations contours, and (iii) instantaneous streamwise vorticity contours.

P1-U15.1 and P1-U25.1 test cases appear to be very similar to the results presented for the P1-U7.4 test case—regions of strong upwash and downwash can be observed close to the wall and these are associated with regions of negative and positive streamwise velocity fluctuations respectively. When the VR is small, the spatial influence of the jet decreases in the vertical direction. This is consistent with the ensemble-averaged streamwise velocity results previously presented in Figs. 11 and 13, where flow structures were observed to flatten towards the wall at small VR.

D. Streamwise entrainment

The downwash and upwash regions presented thus far were observed to be related to the formation of large-scale streamwise flow vortices. In order to assess the entrainment of high momentum ambient fluid into the recirculation region, the entrainment levels across the different test cases are of interest. Conditional averaging was performed by taking the ensemble average of all instances with a negative vertical velocity component (see Berk *et al.* [29]). The conditionally averaged negative vertical velocity was then normalized by the reference velocity (i.e., $-\tilde{V}_{|V<0}/U_{\text{ref}}$) and this parameter served as a proxy for entrainment. The results are presented in Fig. 18 where all contours were plotted with the same range for ease of comparison.

Figures 18(a) (i), 18(b) (i), and 18(c) (i) show the baseline flow without flow control at the $z/H = 0$ measurement plane for all three reference velocities. With the addition of SWJ flow control at position P1 [see Figs. 18(a) (ii), 18(b) (ii), and 18(c) (ii)], higher levels of entrainment can be observed, particularly at regions near the onset of the ramp at $x/H = 0$ and directly above the ramp where the recirculation zone resides [see red box in Figs. 18(a) (ii), 18(b) (ii), and 18(c) (ii)]. When the SWJ actuator was positioned at P2 [see Figs. 18(a) (iii), 18(b) (iii), and 18(c) (iii)], the entrainment levels were much higher even before the tip of the ramp and this persisted after the onset of the ramp. The entrainment in the entire region highlighted by the red box was much higher than when the SWJ flow control was at position P1. This is particularly so for the P2-U7.4 test case as shown in Fig. 18(a) (iii), where high entrainment levels were observed to stick close to the wall of the ramp in the region highlighted by the red box. The increase in entrainment levels associated with actuator position P2 is thought to be due to the formation of secondary flow structures induced by the lifting of strong and large-scale streamwise vortices previously observed in Fig. 15, since they were also observed in the same region close to the wall.

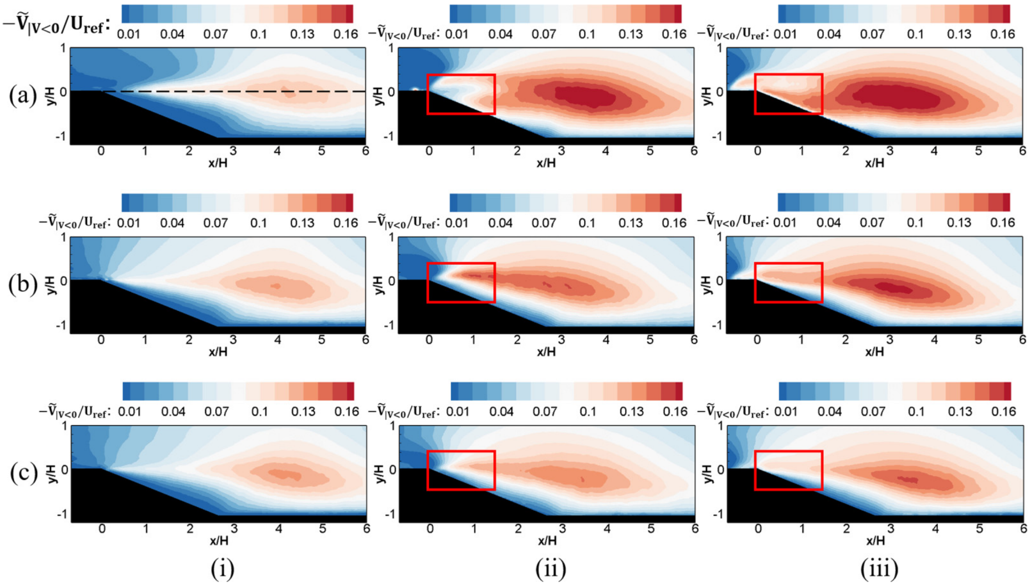

FIG. 18. Entrainment at the $z/H = 0$ measurement plane for (a) $U_{\mathrm{ref}} = 7.4\,\mathrm{m/s}$, (b) $U_{\mathrm{ref}} = 15.1\,\mathrm{m/s}$, and (c) $U_{\mathrm{ref}} = 25.1\,\mathrm{m/s}$ test cases. (i) Baseline without flow control and SWJ at positions (ii) P1 and (iii) P2.

The entrainment extracted along the $y/H = 0$ line [see dashed line in Fig. 18(a) (i)] for all test cases are presented in Fig. 19. For the $z/H = 0$ measurement plane as shown in Fig. 19(a) (i), 19(b) (i), and 19(c) (i), it can be observed that the entrainment levels were almost always higher when the SWJ actuator was positioned at P2. This is especially so in the streamwise range of $0 < x/H < 1$ where the P2-U7.4 test case can be observed to have a sharp spike in entrainment levels [see Fig. 19(a) (i)], and in the streamwise range of $0 < x/H < 0.5$ where the P1-U15.1 and P1-U25.1 test cases were observed to share similar entrainment levels with the baseline [see Figs. 19(b) (i) and 19(c) (i)]. Away from the centerline at measurement planes of $z/H = 1$, 2, and 3 as shown in Figs. 19(a) (ii), 19(b) (ii), and 19(c) (ii), the entrainment levels were higher from approximately $0 < x/H < 2.5$ when the SWJ actuator was positioned at P1.

These results suggest that near the jet centerline, positioning the SWJ actuator at P2 is desirable as it can improve entrainment of high momentum fluid into the recirculation regions. The trend is reversed for measurement planes far from the jet centerline, and it was more desirable to position the SWJ actuator at P1 for higher entrainment levels. This is likely because the secondary flow vortices induced by the primary streamwise vortices (when the actuator is at P2) have limited spanwise coverage, hence they are only able to improve the entrainment levels near the jet centerline. This conclusion is consistent with the earlier ensemble-averaged streamwise results and analysis, as well as the optimal actuator positions presented in Table II.

E. Flow separation delay mechanism

The sweeping frequency in the current study was $\mathrm{St}_{\mathrm{jet}} = 0.018$, or $\mathrm{St}_{\mathrm{H}} = 0.09$ based on the ramp height, which was much lower than the established range of effective forcing frequencies for synthetic jets [29]. For the Strouhal number investigated in the current study, it has been suggested that the rollup of spanwise flow vortices takes a long time and will be completed far downstream of the separation bubble. In contrast, if the Strouhal number matches the shear layer mode ($\mathrm{St}_\theta = 0.011$) or the shedding mode ($\mathrm{St}_{\mathrm{H}} = 0.185$) [42], entrainment levels can be greatly enhanced through the formation of large-scale spanwise vortices and this can improve flow separation control [40]. This begets the question of the flow control mechanism, since the reductions in reattachment length and

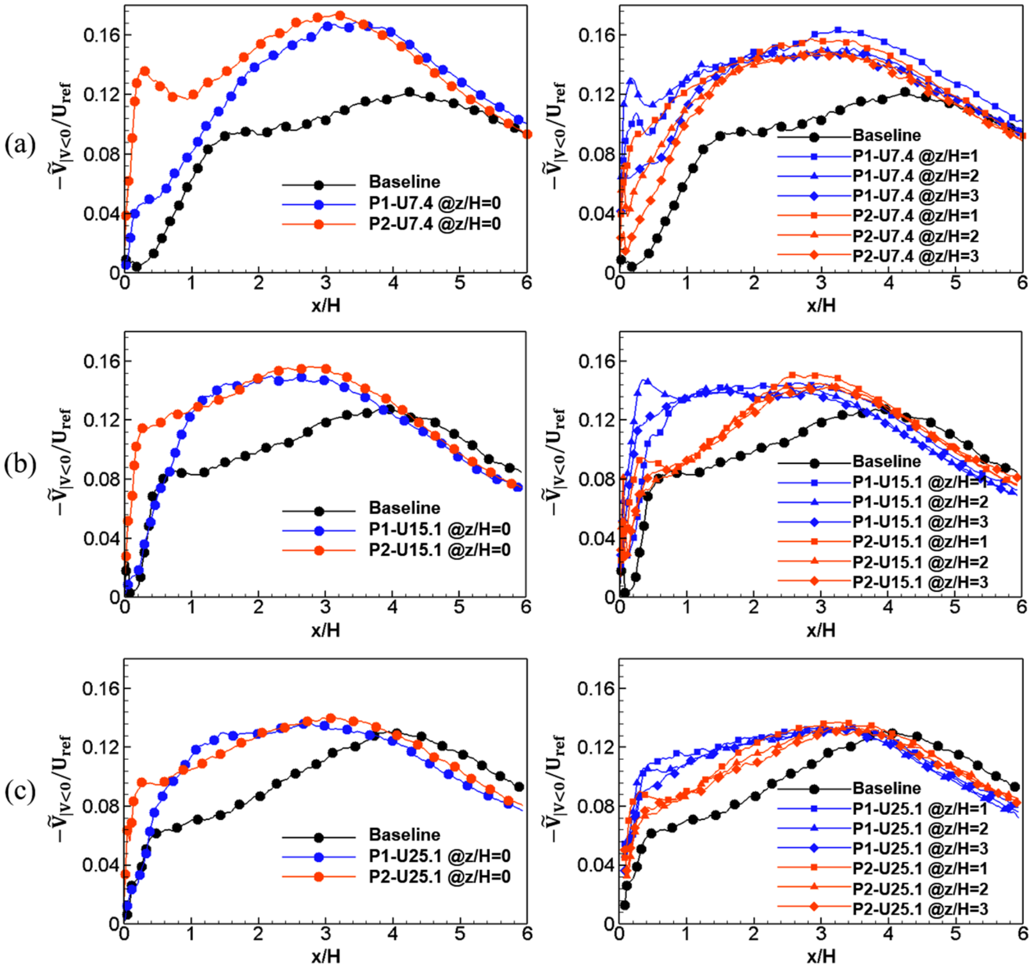

(i) (ii)

FIG. 19. Entrainment extracted along the $y/H = 0$ line for (a) $U_{\mathrm{ref}} = 7.4\,\mathrm{m/s}$, (b) $U_{\mathrm{ref}} = 15.1\,\mathrm{m/s}$, and (c) $U_{\mathrm{ref}} = 25.1\,\mathrm{m/s}$ test cases. Measurement planes at (i) $z/H = 0$ and (ii) $z/H = 1$, 2, and 3.

normalized area of the separation bubble in the current study were comparable with the results of Berk *et al.* [29], where the slot synthetic jet was operated at $\mathrm{St_H} = 0.21$ which was close to the shedding mode frequency.

In this study, the main mechanism in which high momentum ambient fluid was entrained to the low momentum region near the wall is through the formation of streamwise vortices. Depending on the actuator's position, different types of flow vortices dominate the momentum transfer. When the actuator was positioned close to the separating edge at P1, the upwash of the jet and induced downwash produced primary large-scale streamwise vortices. Depending on the phase of the sweep cycle and proximity of the upwash and downwash regions, the primary streamwise flow structures can either form as a single large-scale streamwise vortex with a length scale of close to two jet diameters [see Fig. 14(b)], multiple smaller scale streamwise vortices stacked in the vertical direction and with the same rotation sign [see Fig. 14(a)], or one or more pairs of streamwise vortices that are approximately symmetrical about the upwash of the jet and have opposite sign of rotation [see Fig. 14(c)]. For the last flow scenario, the flow structures are analogous to the legs of hairpin vortices produced from a round synthetic jet [43], although they are not quite the same since the sweeping jet is continuous and the head of the hairpin vortex would not exist. The primary streamwise vortices were observed to be very close to the wall for actuator position P1, hence they are directly responsible for the entrainment of the high momentum ambient fluid into the wall region.

When the actuator was positioned far from the separating edge at P2, the primary streamwise flow structures that were produced were observed to lift off the wall. Secondary flow structures were induced below them leading to the observation of downwash and horizontal velocity fluctuations near the wall. The secondary flow structures were generally weaker than the primary streamwise flow structures, did not have a strong upwash region that is linked to negative streamwise velocity fluctuations, and is likely to be three dimensional without a dominant rotation axis. In this case, since the induced secondary flow structures were very close to the wall, they are chiefly responsible for momentum transfer to the wall region to delay flow separation. The primary streamwise flow structures suffer from a stronger decay in vortex strength due to the larger streamwise advection distance, resulting in limited induction of secondary flow structures far from the jet centerline. Near the jet centerline, they contribute by entraining and supplying high momentum ambient fluid to the secondary streamwise flow structures below. This mechanism is similar to that observed in round synthetic jet flow control, where primary hairpin vortices produced by the jet were observed to induce secondary streamwise vortices below, and the resulting downwash motion of the secondary flow vortices brought high momentum fluid to the wall to delay flow separation [43].

The sweeping jet continuously generates streamwise vortices in a spatially meandering manner. At different phases of the sweep cycle, the primary streamwise vortices that are being produced change in terms of length scale, distribution, and rotation signs, since the regions of strong upwash and downwash constantly change position and relative proximity. Hence, even though the sweeping motion is periodic, irregular three-dimensional flow features are produced (or induced by the primary streamwise vortices) at a low frequency, and this is likely to avoid stabilizing the shear layer while maintaining the capability to increase the near-wall momentum through entrainment of high momentum ambient fluid. This is thought to lead to a more effective and efficient flow separation control method as compared to existing active flow control methods.

The low frequency of the SWJ actuator ($\mathrm{St_H} = 0.09$) did not hinder the formation of the primary streamwise vortices since they are formed by the bulk motion of the fluid due to the strong upwash and downwash regions. This contrasts with the rollup of spanwise flow vortices produced by slot synthetic jets, which relied on processes that required more time and downstream distance to fully develop. Hence, while very low Strouhal numbers ($\mathrm{St_H} = 0.09$) are not ideal for slot synthetic jets [29], they were able to provide effective flow control for a SWJ actuator in the current configuration. This is not to say that the Strouhal number is irrelevant in SWJ flow control for the current configuration, as it may still have influence on the behavior of the primary streamwise vortices, induced secondary flow vortices, flow interactions between adjacent sweeping jet actuators for an array of SWJ actuators, etc. More importantly, the Strouhal number changes the number of primary and secondary streamwise flow structures per unit time that is passing through a fixed location near the separation bubble. This is likely to have an influence on the ensemble-averaged results and the overall flow control effect.

IV. CONCLUSIONS

Flow separation control of a backward-facing ramp using a sweeping jet actuator was investigated experimentally at three different wind tunnel reference velocities ($U_{\mathrm{ref}} = 7.4$, 15.1, and 25.1 m/s), which corresponded to Reynolds numbers based on the boundary layer thickness of $\mathrm{Re}_\delta =$ 2400, 5200, and 9800 and jet-to-reference velocity ratios (VRs) of 1, 0.5, and 0.3 respectively. Apart from the $U_{\mathrm{ref}} = 7.4\,\mathrm{m/s}$ test case which had a transitional-laminar boundary layer, the remaining two test cases had turbulent boundary layers. When flow control was applied at $x/D = -0.9$ (P1) and $x/D = -3.9$ (P2), the size of the separation bubble decreased for all test cases. The largest decrease was observed in the $U_{\mathrm{ref}} = 7.4\,\mathrm{m/s}$ test case, and this was attributed to larger momentum coefficients and better receptivity of transitional-laminar boundary layers to flow control.

At the jet centerline plane and for all three wind tunnel reference velocities, the SWJ actuator performed poorer when it was positioned closer to the separating edge at P1. This was attributed to the influence of a localized low-pressure region created by the sweeping jet in crossflow which, due to its close proximity with the sharp change in ramp geometry, led to a much stronger adverse pressure gradient. The instantaneous cross-stream velocity fluctuations showed a strong relationship between regions of strong upwash and negative streamwise velocity fluctuations, evidencing the detrimental effect of redirecting high momentum fluid upwards and away from the low momentum region near the wall. At large velocity ratios (VR = 1), these effects were accentuated, and an additional secondary separation bubble was observed near the separating edge. In contrast, when the actuator was positioned further upstream at P2, large-scale streamwise vortices produced by the strong downwash and upwash of the jet were observed to lift off the wall, allowing the downwash and spanwise velocity components of induced secondary flow structures to entrain high momentum fluid into the near-wall region. The entrainment levels were generally higher when the actuator was positioned at P2.

Away from the jet centerline, the SWJ actuator performed better when positioned at P1. This was attributed to milder mixing and decay of streamwise vortices, leading to stronger spanwise and downward velocity components and consequently, higher entrainment levels. The spatial influence of the SWJ actuator on the flow field was also observed to be larger when positioned at P1, based on the observation of higher spanwise and vertical velocity components over larger spanwise ranges and with a wider but lower low-pressure region. It is postulated that a critical distance to the separating edge exists, and placement of the SWJ actuator within this critical distance will result in poorer flow control authority especially near the jet centerline axis. This is due to the proximity of the low-pressure region with the separating flow and the region of strong upwash sticking close to the wall. At even higher VR and large ramp angles, the critical distance is postulated to increase further. The pitch, skew, and sweep angles of the SWJ actuator are also expected to play an important role in determining the critical distance.

ACKNOWLEDGMENTS

The authors gratefully acknowledge financial support from the National University of Singapore and would like to express their sincere thanks to Dr. Y. D. Cui from Temasek Laboratories for his support and insightful discussions.

---

[1] M. Sieber, F. Ostermann, R. Woszidlo, K. Oberleithner, and C. O. Paschereit, Lagrangian coherent structures in the flow field of a fluidic oscillator, Phys. Rev. Fluids **1**, 050509 (2016).

[2] S. Aubrun, J. McNally, F. Alvi, and A. Kourta, Separation flow control on a generic ground vehicle using steady microjet arrays, Exp. Fluids **51**, 1177 (2011).

[3] W.-L. Chen, D.-B. Xin, F. Xu, H. Li, J.-P. Ou, and H. Hu, Suppression of vortex-induced vibration of a circular cylinder using suction-based flow control, J. Fluids Struct. **42**, 25 (2013).

[4] V. Uruba, P. Jonáš, and O. Mazur, Control of a channel-flow behind a backward-facing step by suction/blowing, Int. J. Heat Fluid Flow **28**, 665 (2007).

[5] J. Gregory and M. N. Tomac, A review of fluidic oscillator development and application for flow control, in *43rd AIAA Fluid Dynamics Conference* (American Institute of Aeronautics and Astronautics, Inc., Reston, VA, 2013), p. 2474.

[6] M. A. Hossain, R. Prenter, R. K. Lundgreen, A. Ameri, J. W. Gregory, and J. P. Bons, Experimental and numerical investigation of sweeping jet film cooling, J. Turbomach. **140**, 031009 (2018).

[7] X. Wen, Z. Li, W. Zhou, and Y. Liu, Interaction of dual sweeping impinging jets at different reynolds numbers, Phys. Fluids **30**, 105105 (2018).

[8] E. W. Simôes, R. Furlan, R. E. B. Leminski, M. R. Gongora-Rubio, M. T. Pereira, N. I. Morimoto, and J. J. S. Avilés, Microfluidic oscillator for gas flow control and measurement, Flow Meas. Instrum. **16**, 7 (2005).

[9] H. D. Lim, T. H. New, R. Mariani, and Y. D. Cui, Effects of bevelled nozzles on standoff shocks in supersonic impinging jets, Aerosp. Sci. Technol. **94**, 105371 (2019).

[10] M. Y. Andino, J. C. Lin, A. E. Washburn, E. A. Whalen, E. C. Graff, and I. J. Wygnanski, Flow separation control on a full-scale vertical tail model using sweeping jet actuators, in *53rd AIAA Aerospace Sciences Meeting* (American Institute of Aeronautics and Astronautics, Inc., Reston, VA, 2015), p. 0785.

[11] F. Ostermann, R. Woszidlo, C. N. Nayeri, and C. O. Paschereit, Properties of a sweeping jet emitted from a fluidic oscillator, J. Fluid Mech. **857**, 216 (2018).

[12] G. Raman and S. Raghu, Cavity resonance suppression using miniature fluidic oscillators, AIAA J. **42**, 2608 (2004).

[13] R. Woszidlo and I. Wygnanski, Parameters governing separation control with sweeping jet actuators, in *29th AIAA Applied Aerodynamics Conference* (American Institute of Aeronautics and Astronautics, Inc., Reston, VA, 2011), p. 3172.

[14] R. Seele, E. Graff, J. Lin, and I. Wygnanski, Performance enhancement of a vertical tail model with sweeping jet actuators, in *51st AIAA Aerospace Sciences Meeting including the New Horizons Forum and Aerospace Exposition* (American Institute of Aeronautics and Astronautics, Inc., Reston, VA, 2013), p. 0411.

[15] K. Kara, D. Kim, and P. J. Morris, Flow-separation control using sweeping jet actuator, AIAA J. **56**, 4604 (2018).

[16] M. Koklu and L. R. Owens, Comparison of sweeping jet actuators with different flow-control techniques for flow-separation control, AIAA J. **55**, 848 (2017).

[17] M. Koklu and L. R. Owens, Flow separation control over a ramp using sweeping jet actuators, in *7th AIAA Flow Control Conference* (American Institute of Aeronautics and Astronautics, Inc., Reston, VA, 2014), p. 2367.

[18] C. Otto, P. Tewes, J. C. Little, and R. Woszidlo, Comparison between fluidic oscillators and steady jets for separation control, AIAA J. **57**, 5220 (2019).

[19] M. Koklu, Effects of sweeping jet actuator parameters on flow separation control, AIAA J. **56**, 100 (2018).

[20] D. Hirsch and M. Gharib, Schlieren visualization and analysis of sweeping jet actuator dynamics, AIAA J. **56**, 2947 (2018).

[21] M. Shigeta, T. Miura, S. Izawa, and Y. Fukunishi, Active control of cavity noise by fluidic oscillators, Theor. Appl. Mech. Jpn. **57**, 127 (2009).

[22] M. N. Tomac and J. W. Gregory, Phase-synchronized fluidic oscillator pair, AIAA J. **57**, 670 (2019).

[23] S. Gokoglu, M. Kuczmarski, D. Culley, and S. Raghu, Numerical studies of an array of fluidic diverter actuators for flow control, in *41st AIAA Fluid Dynamics Conference and Exhibit* (American Institute of Aeronautics and Astronautics, Inc., Reston, VA, 2011), p. 3100.

[24] X. Wen, J. Liu, Z. Li, D. Peng, W. Zhou, K. C. Kim, and Y. Liu, Jet impingement using an adjustable spreading-angle sweeping jet, Aerosp. Sci. Technol. **105**, 105956 (2020).

[25] F. Ostermann, R. Woszidlo, C. N. Nayeri, and C. O. Paschereit, The interaction between a spatially oscillating jet emitted by a fluidic oscillator and a cross-flow, J. Fluid Mech. **863**, 215 (2019).

[26] S. Zhang and S. Zhong, Turbulent flow separation control over a two-dimensional ramp using synthetic jets, AIAA J. **49**, 2637 (2011).

[27] D. Caruana, F. Rogier, G. Dufour, and C. Gleyzes, The plasma synthetic jet actuator, physics, modeling and flow control application on separation, AerospaceLab, **6**, 1 (2013).

[28] J. McMasters and M. Henderson, Low-speed single-element airfoil synthesis, Technical Soaring **6**, 1 (1980).

[29] T. Berk, T. Medjnoun, and B. Ganapathisubramani, Entrainment effects in periodic forcing of the flow over a backward-facing step, Phys. Rev. Fluids **2**, 074605 (2017).

[30] Y. D. Cui, Z. J. Zhao, J. Li, J. G. Zheng, and B. C. Khoo, Flow separation control over a ramp with nanosecond-pulsed plasma actuators, in *30th International Symposium on Shock Waves Vol. 2*, edited by G. Ben-Dor, O. Sadot, and O. Igra (Springer, New York, 2017).

[31] J. G. Zheng, B. C. Khoo, Y. D. Cui, Z. J. Zhao, and J. Li, Numerical study of control of flow separation over a ramp with nanosecond plasma actuator, Int. J. Mod. Phys.: Conf. Ser. **42**, 1660151 (2016).

[32] A. Kourta, A. Thacker, and R. Joussot, Analysis and characterization of ramp flow separation, Exp. Fluids **56**, 104 (2015).

[33] W. Thielicke and E.J. Stamhuis, PIVlab–towards user-friendly, affordable and accurate digital particle image velocimetry in MATLAB, J. Open Res. Software **2**, e30 (2014).

[34] H. D. Lim, J. Ding, S. Shi, and T. H. New, Proper orthogonal decomposition analysis of near-field coherent structures associated with V-notched nozzle jets, Exp. Therm. Fluid Sci. **112**, 109972 (2020).

[35] T. H. New, S. Shi, and Y. Liu, On the flow behaviour of confined finite-length wavy cylinders, J. Fluids Struct. **54**, 281 (2015).

[36] C. Vanderwel and B. Ganapathisubramani, Effects of spanwise spacing on large-scale secondary flows in rough-wall turbulent boundary layers, J. Fluid Mech. **774**, R2 (2015).

[37] J. Sommeria, UVMAT: A MATLAB program for Particle Imaging Velocimetry (PIV), 2014 (cited 2020 10 February); available at http://servforge.legi.grenoble-inp.fr/projects/soft-uvmat.

[38] H.-J. Schmidt, R. Woszidlo, C. N. Nayeri, and C. O. Paschereit, Separation control with fluidic oscillators in water, Exp. Fluids **58**, 106 (2017).

[39] D. Greenblatt, K. B. Paschal, C.-S. Yao, J. Harris, N. W. Schaeffler, and A. E. Washburn, Experimental investigation of separation control part 1: Baseline and steady suction, AIAA J. **44**, 2820 (2006).

[40] D. Greenblatt, K. B. Paschal, C.-S. Yao, and J. Harris, Experimental investigation of separation control part 2: Zero mass-flux oscillatory blowing, AIAA J. **44**, 2831 (2006).

[41] F. Ostermann, R. Woszidlo, C. Nayeri, and C. O. Paschereit, The time-resolved flow field of a jet emitted by a fluidic oscillator into a crossflow, in *54th AIAA Aerospace Sciences Meeting* (American Institute of Aeronautics and Astronautics, Inc., Reston, VA, 2016), p. 0345.

[42] M. Hasan and A. Khan, On the instability characteristics of a reattaching shear layer with nonlaminar separation, Int. J. Heat Fluid Flow **13**, 224 (1992).

[43] S. Zhong and S. Zhang, Further examination of the mechanism of round synthetic jets in delaying turbulent flow separation, Flow Turbul. Combust. **91**, 177 (2013).